Cell Reports
Medicine

Article

α2δ1-mediated maladaptive sensory plasticity disrupts adipose tissue homeostasis following spinal cord injury

Graphical abstract

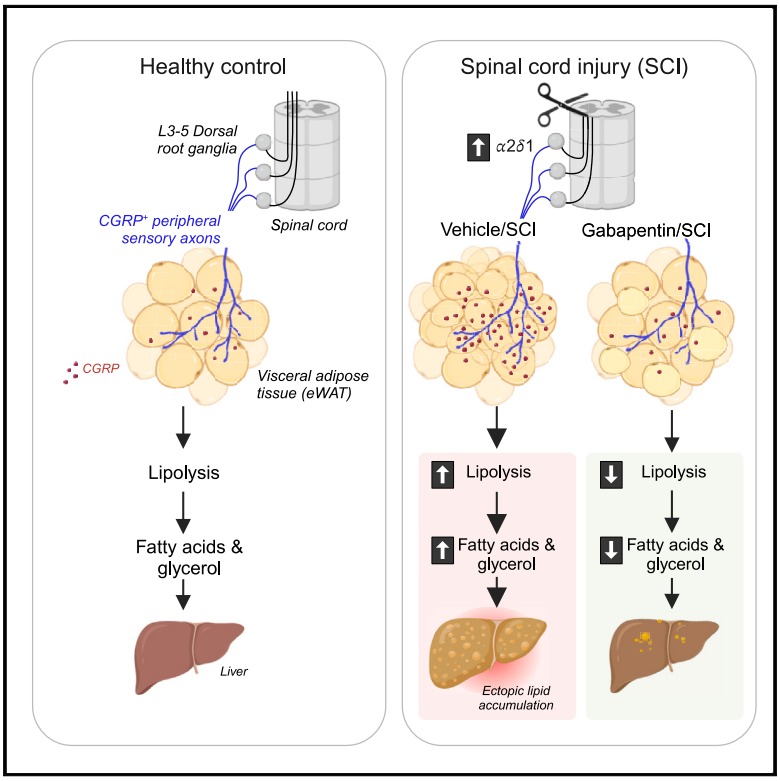

Highlights

- SCI exacerbates lipolysis in epididymal white adipose tissue (eWAT)
- SCI leads to increased α2δ1 expression in CGRP-positive DRG neurons innervating eWAT
- *Cacna2d1* conditional deletion in DRG neurons normalizes eWAT lipolysis after SCI
- α2δ1 blockade via gabapentin administration normalizes eWAT lipolysis after SCI

Authors

Debasish Roy, Elliot Dion, Jesse A. Sepeda, ..., Andrew Sas, Wenjing Sun, Andrea Tedeschi

Correspondence

andrea.tedeschi@osumc.edu

In brief

Roy et al. provide insight into molecular causes and mechanistic underpinning of white adipose tissue dysfunction after spinal cord injury (SCI), facilitating the development of strategies targeting sensory processing to reduce metabolic and cardiovascular complications after SCI.

Roy et al., 2024, Cell Reports Medicine *5*, 101525
May 21, 2024
https://doi.org/10.1016/j.xcrm.2024.101525

CellPress

Cell Reports Medicine

CellPress
OPEN ACCESS

Article

α2δ1-mediated maladaptive sensory plasticity disrupts adipose tissue homeostasis following spinal cord injury

Debasish Roy,[1] Elliot Dion,[1] Jesse A. Sepeda,[2] Juan Peng,[3] Sai Rishik Lingam,[1] Kristy Townsend,[4] Andrew Sas,[2] Wenjing Sun,[1] and Andrea Tedeschi[1,5,6,7,*]

[1]Department of Neuroscience, Wexner Medical Center, The Ohio State University, Columbus, OH 43210, USA
[2]Department of Neurology, Wexner Medical Center, The Ohio State University, Columbus, OH 43210, USA
[3]Center for Biostatistics and Bioinformatics, The Ohio State University, Columbus, OH 43210, USA
[4]Department of Neurological Surgery, Wexner Medical Center, The Ohio State University, Columbus, OH 43210, USA
[5]Chronic Brain Injury Program, The Ohio State University, Columbus, OH 43210, USA
[6]X (formerly Twitter): @TedsunL
[7]Lead contact
*Correspondence: andrea.tedeschi@osumc.edu
https://doi.org/10.1016/j.xcrm.2024.101525

SUMMARY

Spinal cord injury (SCI) increases the risk of cardiometabolic disorders, including hypertension, dyslipidemia, and insulin resistance. Not only does SCI lead to pathological expansion of adipose tissue, but it also leads to ectopic lipid accumulation in organs integral to glucose and insulin metabolism. The pathophysiological changes that underlie adipose tissue dysfunction after SCI are unknown. Here, we find that SCI exacerbates lipolysis in epididymal white adipose tissue (eWAT). Whereas expression of the α2δ1 subunit of voltage-gated calcium channels increases in calcitonin gene-related peptide-positive dorsal root ganglia neurons that project to eWAT, conditional deletion of the gene encoding α2δ1 in these neurons normalizes eWAT lipolysis after SCI. Furthermore, α2δ1 pharmacological blockade through systemic administration of gabapentin also normalizes eWAT lipolysis after SCI, preventing ectopic lipid accumulation in the liver. Thus, our study provides insight into molecular causes of maladaptive sensory processing in eWAT, facilitating the development of strategies to reduce metabolic and cardiovascular complications after SCI.

INTRODUCTION

Individuals sustaining spinal cord injury (SCI) suffer from devastating secondary complications that develop months to years after initial injury. Type 2 diabetes and cardiovascular disease are among the leading causes of death following SCI.[1] Half of SCI individuals experience weight gain attributed to increased adiposity or higher adipose tissue mass.[2,3] Following SCI, increased ectopic lipid deposition is also observed in other organs including the liver, heart, and skeletal muscle.[4–6] Accumulating evidence indicates that pathological ectopic accumulation of triglycerides in non-adipose tissues significantly increases the risk of metabolic and cardiovascular disease after injury.[7,8] During energy deprivation, the adipose tissue mobilizes triglycerides into glycerol and fatty acids via the process of lipolysis, and these are used as fuel for brown adipose tissue, heart, liver, and muscle, thereby maintaining proper energy homeostasis.[9,10] When energy balance becomes dysregulated and adipose tissue no longer can expand in a metabolically healthy way to accommodate increased stored lipid, ectopic lipid accumulation occurs in organs integral to glucose and insulin metabolism, like the liver and muscle, as well as the development of intramuscular adipocytes, and unresolved inflammation contributes to the development of insulin resistance. Thus far, it is not clear whether the underlying cause of metabolic complications after SCI may be linked to dysregulation of lipolysis through altered neural control in adipose tissue. Also unknown are the cellular and molecular mechanisms that cause or contribute to pathophysiological changes in white adipose tissue (WAT) structure and function following SCI.

Both the sympathetic nervous system and sensory neurons with cell bodies located in the dorsal root ganglia (DRG) innervate WAT.[11] Whereas the contribution of sympathetic innervation to WAT function has been well characterized,[12–15] the extent to which sensory innervation drives WAT functions under normal and pathophysiological conditions has remained poorly understood. A number of studies, including ours, have demonstrated a remarkable convergence between structural and functional organization of neuronal circuits and expression of α2δ subunits of voltage-gated calcium channels (VGCC) in neurons.[16–21] α2δ subunits positively regulate neurotransmitter release at presynaptic terminals by increasing plasma membrane expression of VGCC.[22] Of relevance to a potential pathological role of α2δ subunits, expression of neuronal α2δ1 increases following axonal

injury,[23–25] resulting in aberrant sensory activities including chronic pain,[26] hyperexcitability, and epileptiform activity.[27,28]

Here, we show that SCI exacerbates lipolysis in epididymal (e) WAT. Whereas α2δ1 expression increases after a thoracic (T)12 SCI in calcitonin gene-related peptide (CGRP)-positive DRG neurons that project to eWAT, conditional deletion of the gene encoding α2δ1 in these neurons normalizes eWAT lipolysis after SCI. After SCI, α2δ1 pharmacological blockade through systemic administration of gabapentin, a clinically approved drug used to treat neurological disorders, also normalizes eWAT lipolysis, thereby preventing ectopic lipid accumulation in the liver. Thus, our study provides insight into molecular causes and mechanistic underpinning of WAT dysfunction after SCI, facilitating the development of strategies targeting CGRP sensory processing to reduce metabolic and cardiovascular complications after SCI.

RESULTS

SCI exacerbates WAT lipolysis

Given that those individuals that sustained traumatic SCI often experience an increase in adipose tissue mass,[2,3] we questioned whether injury to ascending dorsal column sensory axons following SCI causes structural and functional changes in adipose tissue. To investigate sensory-dependent structural changes in WAT, we subjected adult wild-type (e.g., C57BL/6J fed *ad libitum* with a normal diet) mice to a T12 SCI that completely transected dorsal column sensory axons on one side (Figure 1A) without interrupting sympathetic outflow[29] or impacting sympathetic nerve activity (Figure S1A). Seven days later, we performed histological analysis of WAT depots originating from sham-operated and SCI mice. Whereas no structural changes were observed in subcutaneous WAT (iWAT) after SCI (Figures S1B and S1C), we found an increase in the percentage of small size (<1,000 μm^2) adipocytes in eWAT (Figures 1B and 1C), a phenotype associated with rapid lipid partitioning.[30] Next, we asked whether SCI-related structural remodeling of WAT is coupled with changes in adipose tissue function. Accordingly, we measured WAT lipolysis 7 days after SCI. Our biochemical and immunoblot analysis confirmed that SCI exacerbates lipolysis in eWAT (Figures 1D–1H) but not in iWAT (Figures S1D–S1F). When incubated with the β3 adrenergic agonist isoproterenol to activate lipolysis,[31] eWAT explants from SCI mice increased glycerol release (Figure 1D), suggesting that our experimental model of SCI did not alter sympathetic responsiveness. We corroborated eWAT functional changes by measuring glycerol and free fatty acids in the serum 7 days after SCI. As expected, we found higher levels of glycerol and non-esterified fatty acids in the serum of SCI mice compared to the control (Figure 1I). Elevated non-esterified fatty acids and glycerol levels are indicative of the catabolic release of fatty acids from adipose tissue. Thus, SCI causes acute structural and functional changes in eWAT that may contribute to the development of long-term metabolic and cardiovascular complications.

SCI leads to increased α2δ1 expression in CGRP-positive L3–5 DRG neurons that project to eWAT

Our experimental SCI completely severed sensory ascending dorsal column axons with cell bodies in the lumbar DRG below the injury site. Using a viral-based anterograde tracing strategy, we tested whether DRG neurons with cell bodies in lumbar (L)3–5 DRG, whose centrally projecting axons were severed after a T12 SCI, innervate eWAT. Specifically, we injected adeno-associated viral (AAV) particles expressing the red-shifted fluorescent protein tdTomato into the left sciatic nerve to transduce L3–5 DRG in adult wild-type mice (Figure 2A). Imaging of the unsectioned L4 DRG confirmed a high transduction rate (Figure 2B). Two weeks after AAV injection, we performed a T12 SCI. 7 days after SCI, we isolated and cleared eWAT (left side) after *in toto* staining using an antibody directed against the adipocyte marker perilipin (Figures 2C and 2D). Three-dimensional imaging allowed us to unambiguously visualize tdTomato positive sensory axons originating from injured L3–5 DRG neurons that innervate eWAT (Figure 2D). These axons displayed linear and tortuous trajectories with multiple branching points (Figure 2D). Independent studies reported similar innervation patterns in other WAT depots.[32,33] Axonal varicosities were present along tortuous domains, likely indicating sites of neurotransmitter release (Figure 2D). We corroborated these results by injecting AAV-expressing Cre recombinase fused with eGFP directly into the L4 DRG of adult Ai9 (RCL-tdTomato) mice to trace sensory axons projecting to eWAT (Figures S2A–S2C). As CGRP-positive DRG neurons innervate WAT,[32] we confirmed that L3–5 DRG neurons innervating eWAT express CGRP. We injected the retrograde tracer Fluoro-Gold into the eWAT of adult mice, and 3 days later, we isolated and stained L3–5 DRG. Hence, Fluoro-Gold-positive DRG neurons express CGRP (Figure 2E). After injury, the slow and protracted reorganization of neuronal circuits can promote functional recovery, but it can also cause aberrant neuron firing that eventually culminates in the onset of post-traumatic complications. We and others have demonstrated a remarkable convergence between the rearrangement of neuronal circuits and the expression of neuronal α2δ subunits of VGCC during development and after trauma.[16,19–21,34–36] Of the different α2δ subunits expressed in adult DRG neurons, α2δ1 is the dominant form,[20,37] primarily expressed in nociceptor lineage neurons.[38,39] Given that α2δ subunits positively regulate neurotransmitter release at presynaptic terminals by increasing plasma membrane expression of VGCC,[20,22,40] enhanced α2δ1 expression following axonal injury[26,41] is often associated with aberrant neuron activities.[23–25] In turn, we asked whether α2δ1 expression increases in CGRP-positive L3–5 DRG neurons after SCI. Four days after a T12 SCI, we injected Fluoro-Gold into the lesion site to retrogradely label L3–5 DRG neurons whose centrally projecting axons were severed due to SCI. While no changes were found in large-diameter (>40 μm) L3–5 DRG neurons at 7 days after SCI, our analysis showed that α2δ1 is upregulated in small-diameter (<20 μm) CGRP-positive and medium-diameter (20–40 μm) DRG neurons (Figures 3A and 3B). The expression of the P/Q-type Cav2.1 VGCC is also elevated in small-diameter DRG neurons (Figures 3C and 3D). This is of particular interest as N and P/Q VGCC are responsible for the initiation of synaptic transmission.[42] These channels are often upregulated after nerve injury.[39,43] Concurrently, we found increased CGRP content and increased expression of the CGRP receptor RAMP1 in eWAT 7 days after T12 SCI (Figures 3E–3G). No changes in α2δ2 expression were found in

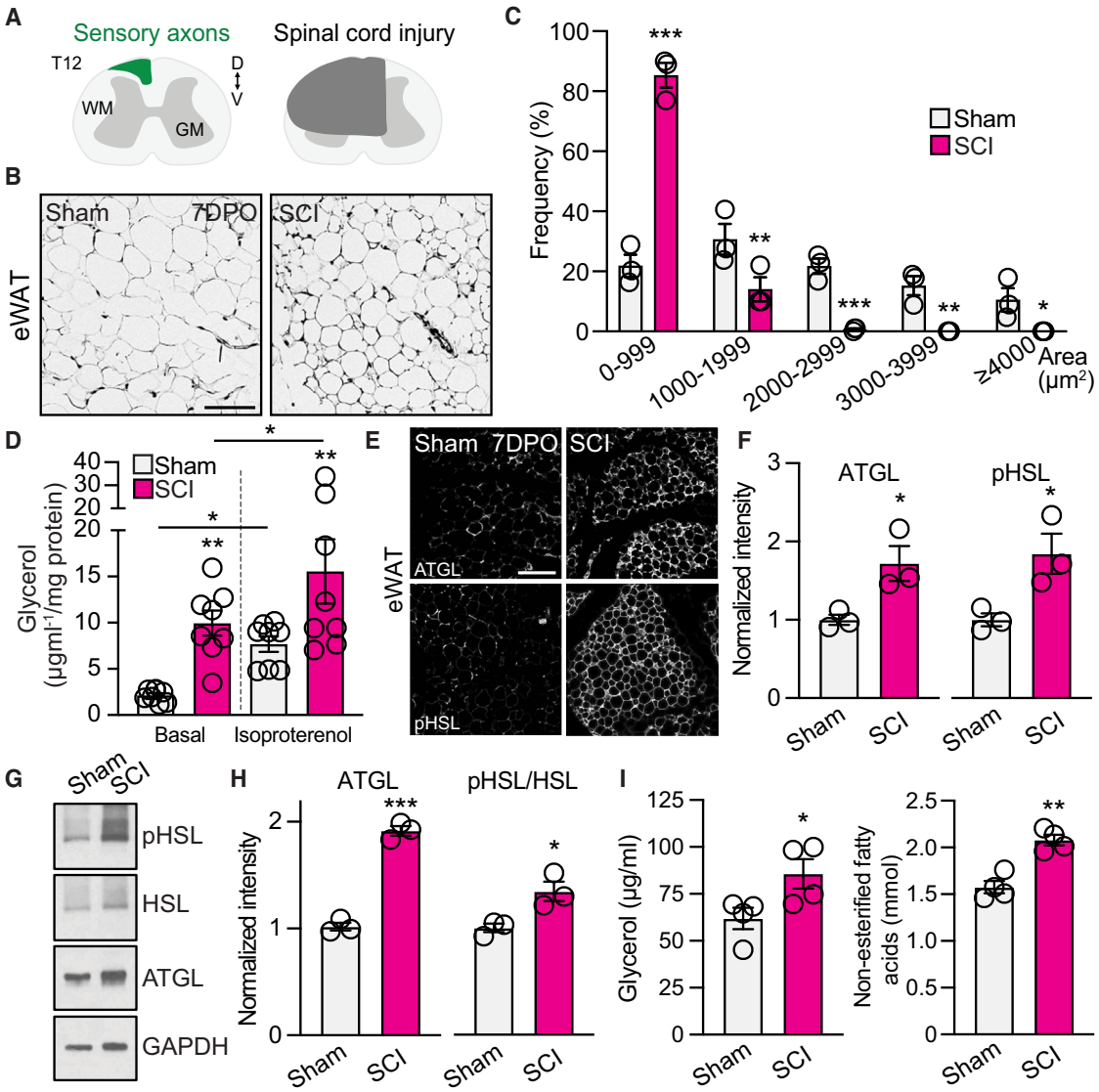

Figure 1. SCI exacerbates eWAT lipolysis

(A) Schematic of T12 SCI.

(B) Representative images of hematoxylin and eosin-stained eWAT sections at 7 days post operation (DPO). Scale, 100 μm.

(C) Quantification of adipocyte area in (B). Mean and SEM (two-way ANOVA $^{*}p < 0.05$, $^{**}p < 0.01$, and $^{***}p < 0.001$, sham $n = 3$ and SCI $n = 3$ biological replicates; 1,376–1,859 adipocytes/experimental condition).

(D) *Ex vivo* eWAT lipolysis at 7DPO under basal (vehicle) and beta-adrenergic receptor-stimulated (isoproterenol, 10 μM) conditions. Mean and SEM (mixed model with a random subject intercept to account for within-subject correlation $^{*}p < 0.05$ and $^{**}p < 0.01$, sham $n = 8$ and SCI $n = 8$ biological replicates).

(E) Representative fluorescence images of eWAT sections at 7DPO. Scale, 100 μm.

(F) Quantification of (E). Mean and SEM (unpaired two-tailed Student's t test $^{*}p < 0.05$, sham $n = 3$ and SCI $n = 3$ biological replicates).

(G) Immunoblots show hormone-sensitive lipase (HSL), phospho (p)HSL, and adipose triglyceride lipase (ATGL) expression in eWAT at 7DPO. HSL and ATGL catalyze the breakdown of triglycerides into glycerol and free fatty acids. GAPDH is used as a loading control.

(H) Quantification of (G). Mean and SEM (unpaired two-tailed Student's t test $^{*}p < 0.05$ and $^{***}p < 0.001$, sham $n = 3$ and SCI $n = 3$ biological replicates).

(I) Glycerol and non-esterified fatty acid concentration in the serum at 7DPO. Mean and SEM (unpaired two-tailed Student's t test $^{*}p < 0.05$ and $^{**}p < 0.01$, sham $n = 4$, and SCI $n = 4$ biological replicates).

Fluoro-Gold retrogradely labeled small-diameter (<20 μm) CGRP-positive L3–5 DRG neurons (mean and SEM: sham = 1,577.18 ± 88.47, SCI = 1,634.89 ± 101.70, unpaired 2-tailed Student's t test $p = 0.679$, sham $n = 4$, and SCI $n = 5$ biological replicates, 1,527–1,740 neurons/experimental condition). To exclude the possibility that increased CGRP content may be caused by the sprouting of CGRP-positive nociceptive nerve terminals in eWAT, we subjected adult $Na_V1.8$-Cre/Ai9(RCL-tdTomato) mice to T12 SCI. Using three-dimensional imaging and reconstruction, we confirmed that centrally projecting,

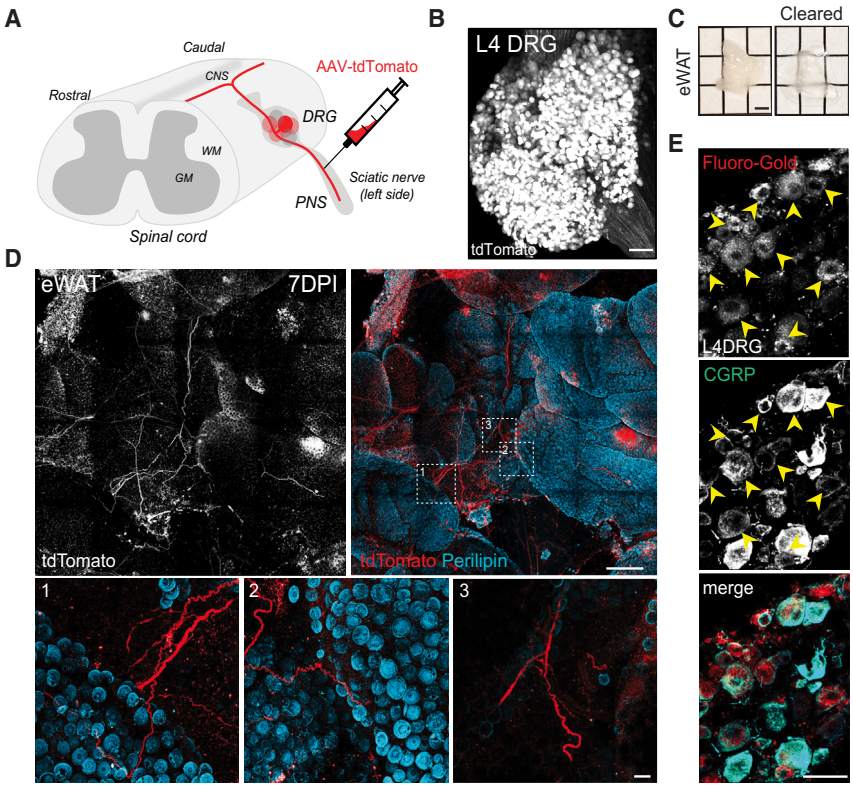

Figure 2. L3–5 DRG neurons innervate eWAT

(A) Schematic of the AAV-based tracing strategy to visualize L3–5 DRG projections to eWAT.

(B) Representative fluorescence image of the unsectioned mouse L4 DRG transduced by AAV-tdTomato. Scale, 100 μm.

(C) Mouse eWAT before and after clearing. Scale, 2 mm.

(D) Representative fluorescence images of the unsectioned mouse eWAT 21 days after AAV injection into the sciatic nerve and 7 days after SCI. Scale, 500 μm (inset: 50 μm).

(E) Representative fluorescence images of L4 DRG. Arrowheads indicate Fluoro-Gold retrogradely labeled CGRP-positive DRG neurons projecting to eWAT. Scale, 50 μm.

tdTomato-positive sensory axons originating from L3–5 DRG in adult $Na_v1.8$-Cre/Ai9(RCL-tdTomato) mice were completely severed after T12 SCI (Figure S3A). Seven days after SCI and sham operation, we isolated and cleared eWAT (left side) and performed three-dimensional imaging of nociceptive nerve terminals. Our analysis indicates that our experimental model of SCI does not alter the density of CGRP-positive nociceptive nerve terminals in eWAT at times when eWAT lipolysis is augmented (Figures 3H and 3I). Furthermore, we isolated and cultured for 48 h DRG neurons originating from L3–5 DRG of $Na_v1.8$-Cre/Ai9(RCL-tdTomato) mice 7 days after sham and SCI. Our analysis of cultured tdTomato-positive DRG neurons did not show clear morphological changes (Figures S3B and S3C). Yet, we found increased expression of Cav2.1 in tdTomato-positive DRG neurons originating from SCI mice (Figures S3D and S3E).

Given that CGRP alone activates lipolysis[44] (Figure 3J) and that calcium influx is known to coordinate the signal transduction regulating lipolysis,[45] we asked whether exposure to CGRP elicits a calcium response in adipocytes in the absence of axonal injury. To test this, we isolated and cultured eWAT primary adipocytes from adult naive mice, and 1 day later, we performed calcium imaging upon CGRP administration. Our data confirm that exposure to CGRP elicited a robust calcium response (Figures 3K–3M), providing evidence that CGRP directly acts on adipocytes. WAT is highly vascularized, and each adipocyte is wrapped by several capillaries. Not only does CGRP activate lipolysis, but it also acts as a potent vasodilator,[46] and changes in adipose tissue microcirculation have been associated with health complications, including adiposity and altered metabolism.[47–49] In turn, we tested whether increased CGRP expression after SCI is associated with hemodynamic changes in eWAT that may contribute to eWAT dysfunction. We subjected adult mice to a T12 SCI or sham operation. Seven days later, we exposed eWAT and performed laser speckle imaging to monitor changes in blood flow. Our results indicate that SCI led to an ~10% increase in blood flow in eWAT (Figures S3F and S3G). By tracing the vasculature down to the capillary level, we discovered that SCI leads to the formation of new blood vessels in eWAT (Figures S3H and S3I). CGRP plays a role in immune response, and WAT releases proinflammatory adipokines that lead to chronic inflammation,[50,51] likely contributing to the deterioration of WAT function and SCI pathophysiology. Accordingly, we performed cell sorting of eWAT samples and discovered that SCI promoted the recruitment of monocytes at 7 days after injury (Figures S3J and S3K). The number of tissue-resident macrophages remained unaltered (Figure S3K). Taken together, these data support the hypothesis that maladaptive changes in CGRP sensory processing are associated with altered eWAT structure and function after SCI in adult mice, thereby providing a genetic entry point to manipulate sensory function for therapeutic gain.

Cacna2d1 conditional deletion in L3–5 DRG neurons normalizes eWAT lipolysis after SCI

To determine whether *Cacna2d1* conditional deletion in DRG neurons that project to eWAT prevents detrimental changes in eWAT after SCI, we injected AAV-expressing Cre recombinase into the left sciatic nerve to transduce L3–5 DRG in adult *Cacna2d1*$^{fl/fl}$ mice (Figure 4A). AAV-GFP was used as a control. *Cacna2d1*$^{fl/fl}$ mice possess *loxP* sites flanking exon 6 of the *Cacna2d1* gene,[52] thus making them a valuable genetic tool to study $\alpha2\delta1$-mediated maladaptive plasticity of the nociceptive pathway in primary sensory neurons. Quantitative PCR analysis of L3–5 DRG (Figure 4B) and immunohistochemistry on virally transduced small-diameter (<20 μm) L3–5 DRG neurons (Figures S4A and S4B) showed a substantial reduction in

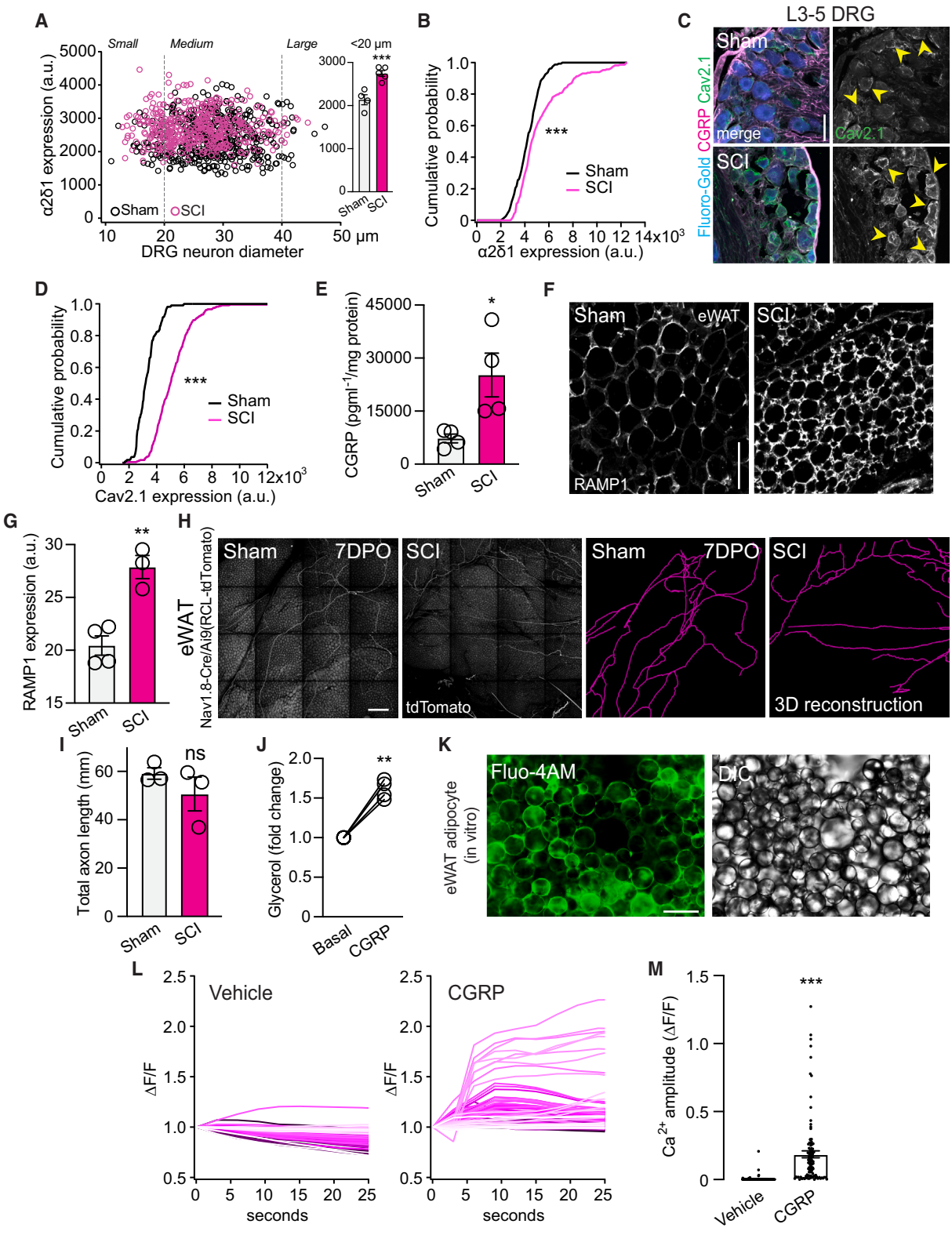

(legend on next page)

Cacna2d1 and α2δ1 expression in mice receiving viral particles expressing Cre. Next, we injected AAV-Cre-eGFP into the left sciatic nerve of adult Ai9 (RCL-tdTomato) mice to determine the percentage of transduced L3–5 CGRP-positive DRG neurons (Figures S4C and S4D). Our data indicate that ~60% of CGRP-positive neurons expressed tdTomato (Figures S4E and S4F), confirming our AAV approach achieved high transduction efficiency. Two weeks after AAV injection into the left sciatic nerve, we performed a T12 SCI, and 7 days later, we ran histological and functional analyses of eWAT originating from *Cacna2d1*$^{fl/fl}$ mice transduced with AAV-Cre and GFP. Strikingly, *Cacna2d1* conditional deletion led to a decrease in the percentage of small-size (<1,000 μm^2) adipocytes in eWAT (Figures 4C and 4D), with a ratio similar to that found in sham-operated mice (Figure 1C). Our biochemical and immunoblot analysis showed that SCI failed to activate the lipolytic machinery in eWAT originating from *Cacna2d1*$^{fl/fl}$ mice transduced with AAV-Cre (Figures 4E–4G). In addition, *Cacna2d1* conditional deletion led to a decrease in CGRP content in eWAT 7 days after SCI (Figure 4H). Of note, *Cacna2d1* conditional deletion did not alter eWAT functional properties in the absence of axonal injury (Figures S4G–S4I). To further test a causal link between α2δ1-dependent maladaptive sensory processing and activation of lipolysis after SCI, we took advantage of another genetic strategy to delete *Cacna2d1* expression in nociceptive DRG neurons. Na$_v$1.8 is a voltage-gated sodium channel, originally thought to be expressed only in a subset of sensory neurons, of which >85% are nociceptors.[53] Further characterization revealed that Na$_v$1.8-Cre is not restricted to nociceptors. It is also expressed by C and Aβ low-threshold mechanoreceptors controlling touch sensation.[54] Nonetheless, low-threshold mechanoreceptors do not innervate eWAT.[32] We subjected adult Na$_v$1.8-Cre/*Cacna2d1*$^{fl/fl}$ mice to a T12 SCI. Na$_v$1.8-Cre mice served as control. Seven days later, we ran histological and functional analysis of eWAT. Once again, *Cacna2d1* deletion led to a decrease in the percentage of small-size (<1,000 μm^2) adipocytes in eWAT (Figures 4I and 4J). Moreover, our biochemical and immunoblot analysis confirmed that SCI failed to engage the lipolytic machinery in eWAT originating from Na$_v$1.8-Cre/*Cacna2d1*$^{fl/fl}$ mice (Figures 4K–4M). We also found a decrease in CGRP content in eWAT originating from Na$_v$1.8-Cre/*Cacna2d1*$^{fl/fl}$ mice (Figure 4N).

Taken together, these data indicate that *Cacna2d1* genetic ablation in DRG neurons prevents α2δ1-dependent maladaptive changes in sensory processing associated with enhanced CGRP release and activation of lipolysis following SCI.

α2δ1 pharmacological blockade via gabapentin administration normalizes eWAT lipolysis after SCI

Gabapentinoids (e.g., gabapentin [GBP] and pregabalin), drugs used clinically to treat various neurological disorders, bind with high affinity and selectivity to α2δ1/2 subunits.[55,56] Accordingly, we tested whether α2δ1 pharmacological blockade through systemic GBP administration could counteract maladaptive changes in sensory processing associated with the activation of lipolysis and ectopic lipid accumulation in organs integral to glucose and insulin metabolism following SCI. We subjected adult mice to T12 SCI or sham operation and chronically administered vehicle (0.9% saline) and GBP (46 mg/kg body weight) starting 1 h after injury until the end of the study (Figure 5A). Under normal physiological conditions, GBP chronic administration over a 1-week period did not alter mouse body weight or eWAT function (Figures S5A–S5D). After SCI, mice administered vehicle and GBP regained body weight to a similar extent with no detectable changes by 2 weeks (Figure 5B). Weight loss after injury is also described in human SCI.[57] During the recovery phase, SCI individuals may be encouraged to increase their caloric intake to offset the initial weight loss. Without adequate nutrition counseling, however, a lowering of the basal metabolic rate in SCI individuals may increase the susceptibility to develop obesity, adiposity, and dyslipidemia.[58,59] We analyzed changes in body composition using EchoMRI and found no changes in lean mass and total body fat when comparing SCI mice administered vehicle and GBP at 4 weeks after SCI (Figure S5E). The

Figure 3. SCI leads to increased α2δ1 and RAMP1 expression in L3–5 DRG neurons and eWAT, respectively

(A) Scatterplot shows α2δ1 expression in Fluoro-Gold retrogradely labeled L3–5 DRG neurons at 7DPO (sham $n = 4$ and SCI $n = 5$ biological replicates, 419–486 neurons/experimental condition). Inset: α2δ1 expression in small-diameter (<20 μm) DRG neurons. Mean and SEM (mixed model with a random subject intercept to account for within-subject correlation $^{***}p < 0.001$).

(B) Distribution of α2δ1 expression in retrogradely labeled CGRP-positive L3–5 DRG neurons at 7DPO. These neurons are a subset of (A) (two-sample Kolmogorov-Smirnov test $^{***}p < 0.001$; sham $n = 4$ and SCI $n = 5$ biological replicates; 161–233 neurons/experimental condition).

(C) Representative fluorescence images of L3–5 DRG at 7DPO. Arrowheads indicate Fluoro-Gold retrogradely labeled CGRP-positive DRG neurons whose centrally projecting axon was severed after SCI. Scale, 50 μm.

(D) Distribution of Cav2.1 expression in retrogradely labeled CGRP-positive L3–5 DRG neurons at 7DPO (two-sample Kolmogorov-Smirnov test $^{***}p < 0.001$; sham $n = 4$ and SCI $n = 5$ biological replicates; 109–236 neurons/experimental condition).

(E) CGRP concentration in eWAT at 7DPO. Mean and SEM (unpaired two-tailed Student's t test $^{*}p < 0.05$, sham $n = 4$ and SCI $n = 4$ biological replicates).

(F) Representative fluorescence images of eWAT at 7DPO. Scale, 100 μm.

(G) Quantification of (F). Mean and SEM (unpaired two-tailed Student's t test $^{**}p < 0.01$, sham $n = 4$ and SCI $n = 3$ biological replicates).

(H) Representative fluorescence images and 3D reconstruction of nociceptive nerve terminals in the unsectioned eWAT at 7DPO. Scale, 500 μm.

(I) Quantification of (H). Mean and SEM (unpaired two-tailed Student's t test, ns [not significant], sham $n = 3$ and SCI $n = 3$ biological replicates).

(J) *ex vivo* eWAT lipolysis under basal (vehicle) and CGRP-stimulated (1 μM) conditions. Scatterplot shows fold change in glycerol release (paired two-tailed Student's t test $^{**}p < 0.01$, $n = 4$ biological replicates).

(K) Representative fluorescence and DIC images of cultured adult eWAT adipocytes loaded with the calcium indicator Fluo-4 AM. Scale, 100 μm.

(L) Calcium response in primary eWAT adipocyte after vehicle (dH_2O) and CGRP (43 μM) administration (vehicle $n = 81$ and CGRP $n = 100$ eWAT adipocyte traces from 5 independent experiments/experimental condition).

(M) Quantification of (L). Mean and SEM (unpaired two-tailed Student's t test $^{***}p < 0.001$, vehicle $n = 81$ and CGRP $n = 100$ eWAT adipocyte traces from 5 independent experiments/experimental condition).

CellPress
OPEN ACCESS

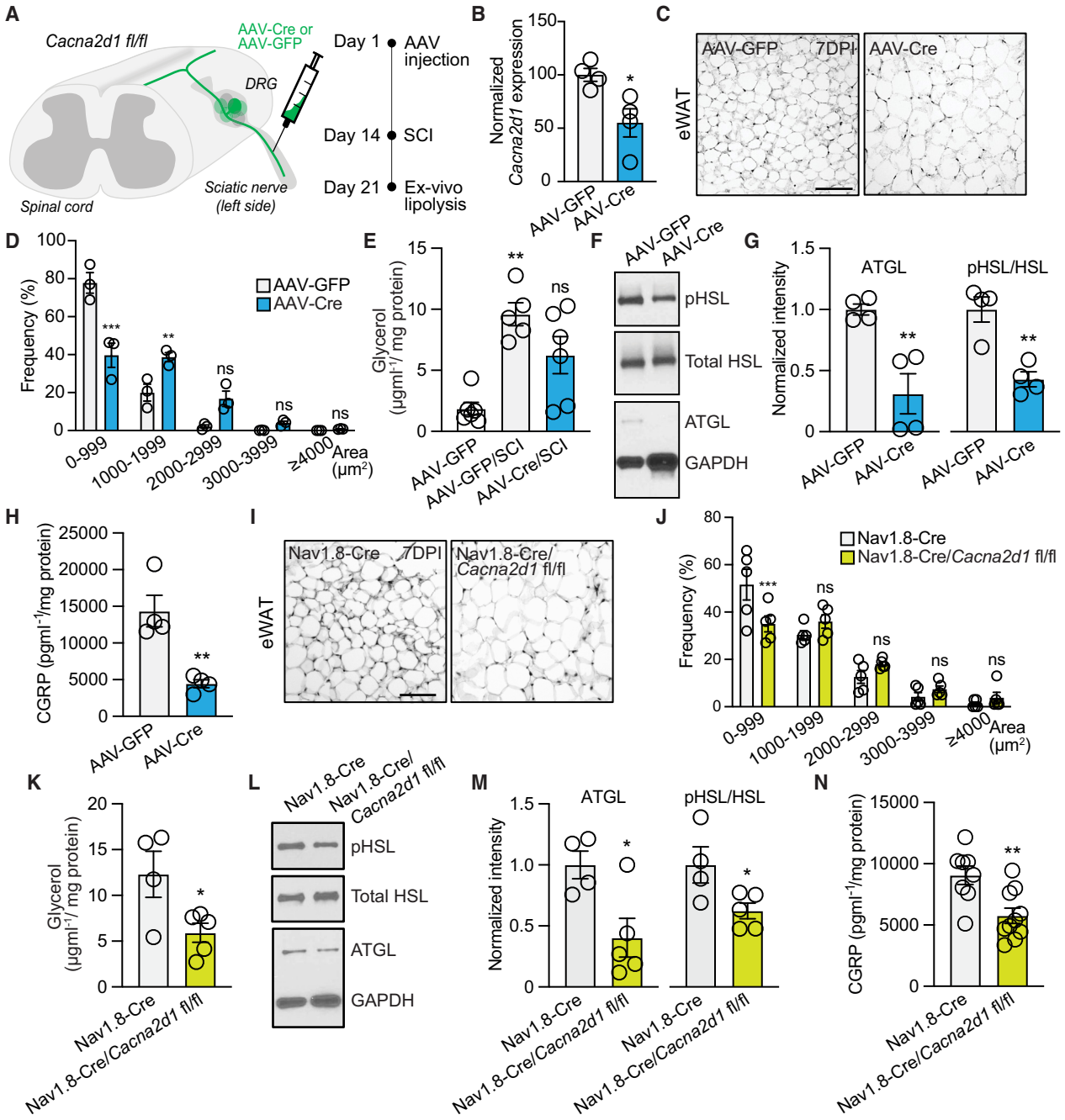

Figure 4. *Cacna2d1* conditional deletion in DRG neurons normalizes eWAT lipolysis after SCI

(A) Experimental scheme and timeline of AAV injection to transduce L3–5 DRG.

(B) Real-time qPCR shows *Cacna2d1* normalized expression in adult L3–5 DRG from *Cacna2d1*$^{fl/fl}$ mice injected with either AAV-GFP or AAV-Cre. Mean and SEM (unpaired two-tailed Student's t test *$p < 0.05$, AAV-Ctr $n = 4$ and AAV-Cre $n = 4$ biological replicates).

(C) Representative hematoxylin and eosin images of eWAT at 7 days post injury (DPI). Scale, 100 μm.

(D) Quantification of adipocyte area in (C). Mean and SEM (two-way ANOVA **$p < 0.01$ and ***$p < 0.001$, ns [not significant], AAV-GFP/SCI $n = 3$ and AAV-Cre/SCI $n = 3$ biological replicates; 2,063–2,322 adipocytes/experimental condition).

(E) *Ex vivo* eWAT lipolysis at 7DPI. Mean and SEM (Kruskal-Wallis test followed by Dunn's multiple comparisons test **$p < 0.01$, ns [not significant], AAV-GFP $n = 6$, AAV-GFP/SCI $n = 5$, and AAV-Cre/SCI $n = 6$ biological replicates). The AAV-GFP samples are the same as in Figure S4E.

(F) Immunoblots show pHSL, HSL, and ATGL expression in eWAT at 7DPI. GAPDH is used as a loading control.

(G) Quantification of (F). Mean and SEM (unpaired two-tailed Student's t test **$p < 0.01$, AAV-GFP/SCI $n = 4$ and AAV-Cre/SCI $n = 4$ biological replicates).

(legend continued on next page)

fact that our experimental model of incomplete SCI allows mice to substantially regain ground locomotion within days after injury may provide a plausible explanation as to why we failed to observe changes in body composition 1 month post SCI. We then ran histological analysis of eWAT and found that GBP chronic administration led to a decrease in the percentage of small-size (<1,000 μm^2) adipocytes (Figures 5C and 5D) to an extent similar to that found after *Cacna2d1* deletion (Figure 4D). Our biochemical and immunoblot analysis showed that mice administered GBP normalized lipolysis (Figures 5E–5H), as shown by the reduction in glycerol released from eWAT and in the serum (Figures 5E and 5F). In addition, $\alpha2\delta1$ pharmacological blockade via GBP administration led to a decrease in CGRP content in the serum 7 days after SCI (Figure 5I). We also found that GBP chronic administration prevented ectopic lipid accumulation in the liver 1 month after SCI (Figures 5J and 5K). However, prolonged GBP administration negatively impacted insulin tolerance (Figure S5F), likely by blocking $\alpha2\delta1$ in neurons of the ventromedial hypothalamus.[60] Along this line, a previous study reported that conventional $\alpha2\delta1$-null mice show increased susceptibility to develop diabetes.[61] Given that prolonged GBP administration after SCI did not alter pancreas structure and function (Figures S5G and S5H), we evaluated the extent to which gradual interruption of the medication may be necessary to prevent potential side effects associated with the long-term use of gabapentinoids while still preventing ectopic lipid deposition in the liver 1 month after SCI. We subjected another cohort of adult mice to T12 SCI and gradually discontinued the GBP treatment over 4 weeks after SCI. Strikingly, discontinued (d) GBP treatment effectively prevented ectopic lipid deposition in the liver 31 days after SCI (Figures S5I and S5J) and normalized insulin tolerance (Figure S5K). None of our experimental conditions impacted glucose tolerance at 30–34 days after SCI (Figure S5L). Using metabolic cages to measure energy expenditure, we found no major changes in oxygen consumption in any of the experimental conditions we tested. However, SCI mice as well as vehicle/SCI and GBP/SCI were subjected to greater changes in energy expenditure while transitioning to the dark cycle (e.g., active state) 1 month after SCI (Figure 5L). Oxygen consumption in dGBP/SCI was more like sham-operated mice. The respiratory exchange rate indicated that all experimental conditions except the sham and dGBP/SCI groups were subjected to greater changes while transitioning to the active state at 1 month after operation, indicating that carbohydrates are being predominantly used for fuel as opposed to lipids during lipid oxidation and that dGBP better normalizes energy expenditure after SCI.

Altogether, these data provide evidence that $\alpha2\delta1$ pharmacological blockade through GBP administration regularizes eWAT lipolysis and metabolism after SCI, highlighting the potential for repurposing gabapentinoids as a promising treatment strategy to counteract eWAT dysfunction after SCI.

Cacna2d1 deletion and $\alpha2\delta1$ pharmacological blockade converge onto a specific eWAT gene signature

To gain mechanistic insight into the molecular signature underlying the beneficial action on eWAT function of *Cacna2d1* deletion in L3–5 DRG neurons and $\alpha2\delta1$ pharmacological blockade via GBP administration after SCI, we turned to analysis of gene expression. We prioritized a gene list comprising inflammatory players (*Nlrp3*, *Ccl2*, *Il1b*, *Tnfa*, *F4/80*, and *Il6*), key regulators of *de novo* lipogenesis (*Acaca*, *Fasn*, *Srebp1c*, and *Chrebp1b*), adipocyte differentiation and insulin sensitivity (*Adipoq*), energy homeostasis (*Leptin*), lipid binding and uptake (*Fabp4*, *Lpl*, and *Cd36*), triglyceride synthesis enzymes (*Dgat1* and *Dgat2*), and a master transcription regulator of lipid metabolic pathways (*Pparg*). At 7 days after sham operation and SCI, we collected eWAT samples, extracted RNA, and prepared it for RT-qPCR. Whereas SCI led to increased expression of *Tnfa*, *Leptin*, *Srebp1c*, *Fasn*, *Pparg*, and *Adipoq*, *Cacna2d1* deletion and $\alpha2\delta1$ pharmacological blockade via GBP administration lowered the expression of *Leptin*, *Lpl*, *Dgat2*, *Srebp1c*, *Acaca*, and *Fasn* (Figures 6A and 6B). When comparing the three experimental conditions, a common gene signature emerged further confirming the effectiveness of our experimental approaches in normalizing eWAT function. The expression of *Leptin*, *Srebp1c*, and *Fasn* increased in eWAT 7 days after SCI. In contrast, virally mediated *Cacna2d1* deletion in L3–5 DRG neurons and $\alpha2\delta1$ pharmacological blockade via GBP administration led to a reduction in *Leptin*, *Srebp1c*, and *Fasn* expression in eWAT 7 days after SCI (Figures 6A and 6B). Leptin is a hormone released by adipose tissue that regulates energy expenditure. As the amount of leptin in the blood is proportional to the amount of adipose tissue, an increase in body fat often results in high levels of leptin (hyperleptinemia) that can cause leptin resistance. Hyperleptinemia is associated with health complications including SCI[62] and nonalcoholic fatty liver disease.[63] SREBP1c encodes a basic helix-loop-helix-leucine zipper transcription factor that binds to the sterol regulatory element-1 in the promoter of genes involved in sterol biosynthesis and lipid homeostasis.[64] Increased SREBP1c expression contributes to elevate hepatic fatty acid synthesis leading to steatosis in diabetic mice and rats.[65–67] FASN is a multifunctional enzyme that catalyzes *de novo* biosynthesis of long-chain saturated fatty

(H) CGRP concentration in eWAT at 7DPI. Mean and SEM (unpaired two-tailed Student's t test $^{**}p < 0.01$, AAV-GFP/SCI $n = 4$ and AAV-Cre/SCI $n = 4$ biological replicates).
(I) Representative hematoxylin and eosin images of eWAT at 7DPI. Scale, 100 μm.
(J) Quantification of adipocyte area in (I). Mean and SEM (two-way ANOVA $^{***}p < 0.001$, ns [not significant], $Na_v1.8$-Cre $n = 5$ and $Na_v1.8$-Cre/*Cacna2d1* fl/fl $n = 5$ biological replicates; 2,732–3,170 adipocytes/experimental condition).
(K) *Ex vivo* eWAT lipolysis at 7DPI. Mean and SEM (unpaired two-tailed Student's t test $^{*}p < 0.05$, $Na_v1.8$-Cre $n = 4$ and $Na_v1.8$-Cre/*Cacna2d1* fl/fl $n = 5$ biological replicates).
(L) Immunoblots show pHSL, HSL, and ATGL expression in eWAT at 7DPI. GAPDH is used as a loading control.
(M) Quantification of (L). Mean and SEM (unpaired two-tailed Student's t test $^{*}p < 0.05$, $Na_v1.8$-Cre $n = 4$ and $Na_v1.8$-Cre/*Cacna2d1* fl/fl $n = 5$ biological replicates).
(N) CGRP concentration in eWAT at 7DPI. Mean and SEM (unpaired two-tailed Student's t test $^{**}p < 0.01$, $Na_v1.8$-Cre $n = 8$ and $Na_v1.8$-Cre/*Cacna2d1* fl/fl $n = 10$ biological replicates).

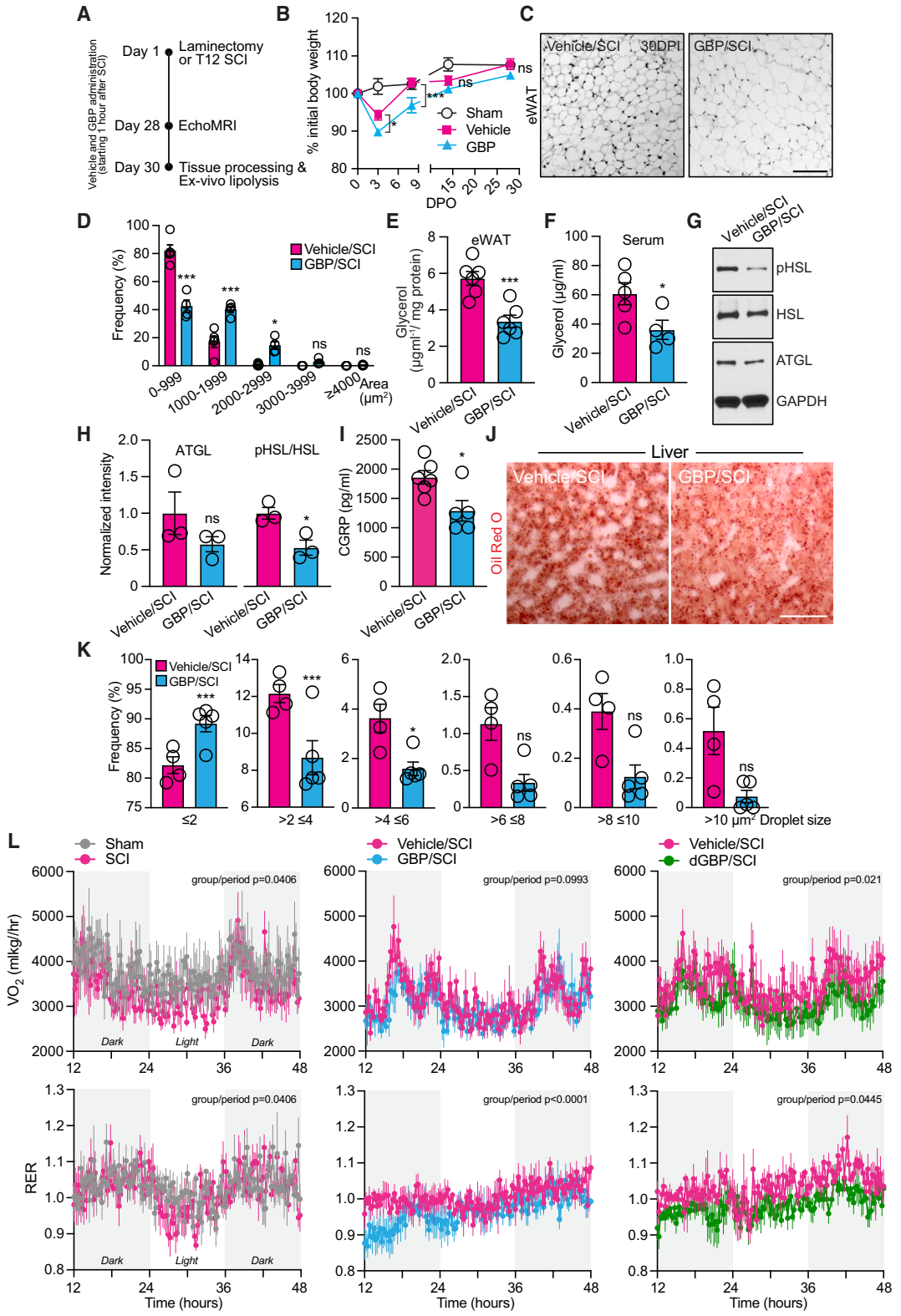

(legend on next page)

acids. FASN overexpression and hyperactivity are often associated with tumor growth.[68] Expressions of FASN and its main transcriptional regulator SREBP1 are also elevated in liver biopsies from nonalcoholic fatty liver disease patients.[69] When compared to *Cacna2d1* deletion, a greater gene signature is associated with GBP administration. This may not be surprising as the medication is administered systemically and, therefore, can exert its action on supraspinal sites, including the hypothalamus. Unexpectedly, α2δ1 pharmacological blockade led to increased expression of the inflammatory markers *Nlrp3*, *Il1b*, and *Tnfa* (Figures 6A and 6B). Next, we took advantage of a biological database to predict protein-protein interaction and hierarchical network organization. As input, we entered the gene signature shared between *Cacna2d1* deletion and α2δ1 pharmacological blockade (Figure 6C) and centered the network on each of the differentially expressed genes (DEGs) (e.g., *Leptin*, *Fasn*, and *Srebp1c*) in common with all three experimental conditions to identify first neighbors (Figure 6D). AMPK signaling pathway, insulin signaling, and fatty acid biosynthesis are among the top three terms in our enrichment analysis (Table S1). Together, these data provide evidence that *Cacna2d1* deletion and α2δ1 pharmacological blockade via GBP administration exert their beneficial action on eWAT function by, at least in part, suppressing a gene signature centered on *de novo* lipogenesis, energy expenditure, and transcriptional regulation of lipid metabolic pathways.

DISCUSSION

Accumulating evidence suggests that pathological expansion of adipose tissue and ectopic lipid accumulation after SCI increases the risk of cardiometabolic disorders, including hypertension, dyslipidemia, and insulin resistance.[70] In this study, we provide evidence that α2δ1 hijacks eWAT function by inducing maladaptive sensory processing after SCI. Given that α2δ1 is targeted by a class of clinically approved drugs, our study identifies a genetic entry point and a druggable target that can be manipulated to prevent long-term chronic metabolic complications, thereby improving neurological function and enhancing the quality of life after SCI.

While the contribution of sympathetic nerves in controlling WAT function is well established,[12–15] our current understanding of the physiological role of sensory nerves in steering WAT function under normal and pathophysiological conditions is fragmentary. A recent study underscores the importance of somatosensory innervation of iWAT under normal physiological conditions.[32] To investigate the relationship between maladaptive changes in sensory processing and eWAT dysfunction after SCI, we used an experimental model that completely severs sensory ascending axons at T12 without interrupting or impacting sympathetic nerve activity in adult mice.[29] At 7 days after SCI, eWAT undergoes structural changes typically associated with rapid lipid partitioning.[30] Hence, we discovered that SCI leads to increased lipid mobilization by lipolysis from eWAT in adult mice. Using biochemical, histological, and molecular assays, we found that the expression of adipose triglyceride lipase, the rate-limiting enzyme that catalyzes the breakdown of triglycerides in adipose tissue,[71] is upregulated after SCI. Interestingly, we did not find structural changes in iWAT, indicating that WAT dysfunction may be dependent on the injury level. Whether adipose tissue depots throughout the body may be targeted in an SCI level-dependent fashion remains to be tested.

After injury, maladaptive reorganization of neuronal circuits causes aberrant neuron firing that eventually culminates in the onset of post-traumatic disorders. Accumulating evidence underscores a remarkable convergence between the rearrangement of neuronal circuits and the expression of neuronal α2δ subunits of VGCC during development and after trauma.[16,19–21,34–36] While studying the mechanisms underlying maladaptive changes in sensory processing causing or contributing to eWAT dysfunction after SCI, we discovered that α2δ1 expression increases in CGRP-positive DRG neurons located below the site of injury. Given that α2δ subunits positively regulate neurotransmitter release at presynaptic terminals by increasing plasma membrane expression of VGCC,[20,22,40] enhanced α2δ1 expression following trauma is often associated with aberrant neuron activities.[26–28]

Figure 5. α2δ1 pharmacological blockade via GBP administration normalizes eWAT lipolysis and reduces ectopic lipid accumulation in the liver after SCI

(A) Experimental scheme.

(B) Mouse body weight. Mean and SEM (mixed model with a random subject intercept to account for within-subject correlation $*p < 0.05$ and $***p < 0.001$, ns [not significant], sham $n = 10$, vehicle/SCI $n = 11$, and GBP/SCI $n = 11$ biological replicates).

(C) Representative images of hematoxylin and eosin-stained eWAT sections 28DPO. Scale, 100 μm.

(D) Quantification of adipocyte area in (C). Mean and SEM (two-way ANOVA $*p < 0.05$ and $***p < 0.001$, ns [not significant], vehicle/SCI $n = 5$ and GBP/SCI $n = 4$ biological replicates; 654–1,051 adipocytes/experimental condition).

(E) *Ex vivo* eWAT lipolysis at 30DPI (unpaired two-tailed Student's t test $***p < 0.001$, vehicle/SCI $n = 6$ and GBP/SCI $n = 6$ biological replicates).

(F) Glycerol concentration in the serum at 30DPI. Mean and SEM (unpaired two-tailed Student's t test $*p < 0.05$, vehicle/SCI $n = 5$ and GBP/SCI $n = 4$ biological replicates).

(G) Immunoblots show pHSL, HSL, and ATGL expression in eWAT at 30DPI. GAPDH is used as a loading control.

(H) Quantification of (G). Mean and SEM (unpaired two-tailed Student's t test $*p < 0.05$, ns [not significant], vehicle/SCI $n = 3$ and GBP/SCI $n = 3$ biological replicates).

(I) CGRP concentration in the serum at 7DPI. Mean and SEM (unpaired 2-tailed Student's t test $*p < 0.05$, vehicle/SCI $n = 6$ and GBP/SCI $n = 5$ biological replicates).

(J) Representative images of liver sections stained with oil red O to visualize lipid accumulation. Scale, 50 μm.

(K) Quantification of (J). Mean and SEM (two-way ANOVA $*p < 0.05$ and $***p < 0.001$, ns [not significant], vehicle/SCI $n = 4$ and GBP/SCI $n = 5$ biological replicates).

(L) Metabolic cage assessment (CLAMS) of oxygen consumption (VO_2) and respiratory exchange rate (RER) at 1 month after SCI. Mean and SEM (mixed model with a random subject intercept to account for within-subject correlation, p values for group/period interaction are provided, sham $n = 4$, SCI $n = 4$, vehicle/SCI (middle) $n = 4$, GBP/SCI $n = 5$, vehicle/SCI (right) $n = 4$, and dGBP/SCI $n = 5$).

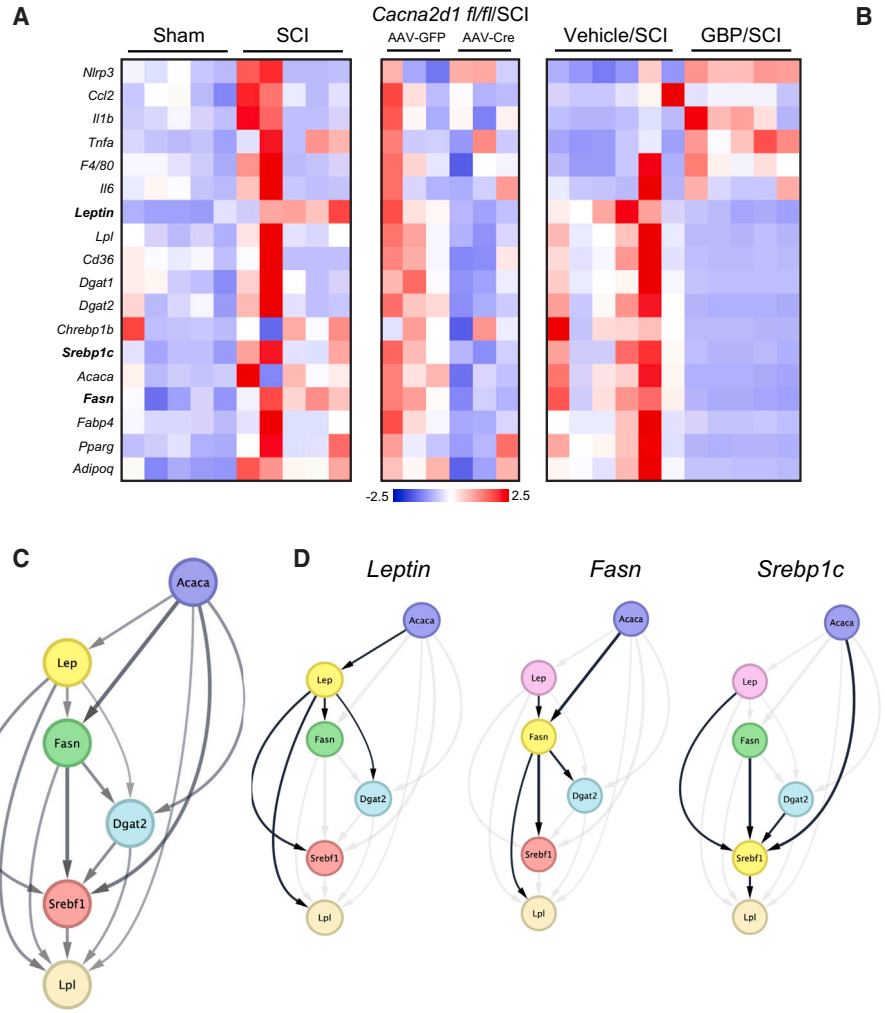

Figure 6. eWAT gene signature associated with *Cacna2d1* conditional deletion in DRG neurons and α2δ1 pharmacological blockade via GBP administration after SCI

(A) eWAT gene expression at 7DPO analyzed by RT-qPCR. Genes in bold showed differential expression in all experimental conditions. Z transformed blue to red.

(B) List of DEG associated to the experimental conditions in (A) (unpaired two-tailed Student's t test, sham $n = 5$, SCI $n = 5$, AAV-GFP/SCI $n = 3$, AAV-Cre/SCI $n = 3$, vehicle/SCI $n = 6$, and GBP/SCI $n = 5$ biological replicates).

(C) Hierarchical structure of functional protein association network predicted by STRING.

(D) Identification of first neighbors in (C).

Using anterograde and retrograde viral tracing strategies, we demonstrated CGRP-positive DRG neurons located below the site of injury project to eWAT. Elevation of α2δ1 expression in these neurons is associated with increased CGRP content and increased expression of the CGRP receptor RAMP1 in eWAT. We excluded the possibility that increased CGRP content after SCI was caused by the sprouting of CGRP-positive nociceptive nerve terminals in eWAT. In fact, no changes in the density of nociceptive nerve fibers were found in eWAT at times when lipolysis was exacerbated. Given that CGRP alone can drive *ex vivo* lipolysis in the absence of SCI and that CGRP directly acts on eWAT adipocytes as shown by the robust calcium response elicited in primary eWAT adipocytes upon CGRP exposure, our findings indicate maladaptive sensory processing actively contributes to eWAT dysfunction after SCI. A comprehensive characterization of the electrophysiological properties, calcium dynamics, and transcriptional signatures associated with SCI-dependent maladaptive sensory processing in CGRP-positive DRG neurons that project to eWAT will be an important direction for future investigations.

Although adipocytes account for most of the volume of eWAT, they only make up ~50% of its cellular content. A stromal vascular fraction, including immune cells, fibroblasts, adipocyte precursors, and vascular cells, densely populates eWAT. Accumulating evidence indicates that changes in WAT microcirculation and inflammation are associated with adiposity, insulin resistance, and altered metabolism.[48,51,72] Not only CGRP alone drives lipolysis, it also functions as a potent vasodilator.[46] Using

a vasculature tracing method and functional imaging,[73] we found that SCI leads to increased blood flow and the formation of new blood vessels in eWAT. An in-depth characterization of the changes in vasculature permeability and its contribution to inflammation awaits further testing. After SCI, WAT releases proinflammatory adipokines that lead to chronic inflammation,[74] thereby contributing to the deterioration of WAT function and SCI pathophysiology. Using a cell-sorting strategy, we discovered SCI led to monocyte recruitment to eWAT. Whereas the recruitment of monocytes is key for effectively controlling infections,[75] recruited monocytes can be deleterious and cause or contribute to immunopathology after SCI. Whether CGRP contributes to neurogenic inflammation and alters the behavior of stromal cells, including contractile mural cells of blood microvessels, remain to be tested.

To normalize eWAT function after SCI, we used genetic and pharmacological approaches targeting *Cacna2d1* and α2δ1, respectively. *Cacna2d1* conditional deletion in adult L3–5 DRG neurons that project to eWAT prevents eWAT structural changes, leading to a normalization, at least in part, of lipolysis. We generated the same conclusion using another genetic strategy that allowed us to conditionally delete *Cacna2d1* from nociceptive DRG neurons. *Cacna2d1* conditional deletion also results in a reduction of CGRP content in eWAT, presumably by dampening presynaptic terminal release. As AAV vectors are becoming the leading platform for gene replacement, silencing, and editing,[76] continuous expansion of AAV biology may offer opportunities for the development of *Cacna2d1* gene targeting approaches in humans. If successfully developed and tested *in vivo*, therapeutic applications using CGRP antagonists[77] may provide a valuable alternative to normalize eWAT function after SCI. Chemically induced ablation of sensory innervation via local administration of capsaicin has been shown to protect from glucose intolerance in a mouse model of obesity.[32] Whether the same strategy may be effective in suppressing aberrant sensory activity and normalizing eWAT function after SCI awaits further testing.

α2δ1 pharmacological blockade via administration of clinically approved GBP also normalizes eWAT structure and function, thereby preventing ectopic lipid deposition in the liver after SCI. Strikingly, suppression of a common gene signature centered on *de novo* lipogenesis, energy expenditure, and transcriptional regulation of lipid metabolic pathways underscores the beneficial action of *Cacna2d1* conditional deletion in L3–5 DRG neurons and α2δ1 pharmacological blockade on eWAT function after SCI.

We administered GBP in mice at the clinically relevant dose of 46 mg/kg that converts to a 3.73 mg/kg in humans.[78] For an average 60-kg individual, the corresponding GBP dosage of 223.8 mg is well within the most common GBP dosing range in humans.[79] Dizziness, drowsiness, water retention, and weight gain are common side effects associated with prolonged GBP systemic administration in humans. Knowing when to gradually stop the medication without losing its beneficial effect is key. Along this line, our data provide evidence that gradual interruption of GBP administration over 4 weeks after SCI prevents complications related to insulin resistance while retaining its beneficial action in preventing ectopic lipid deposition in the liver. Alternatively, the use of tunable, local drug delivery systems will not only increase the drug targeting efficacy but will also circumvent unwanted side effects and misuse associated with systemic GBP administration.[80]

Whereas the beneficial action of gabapentinoids in promoting neurological recovery after SCI is gaining support,[16,19,81,82] overcoming side effects associated with prolonged GBP administration and polypharmacy in SCI individuals[83] must be investigated before embarking on clinical trials in humans.

In summary, our data provide insight into the cell biology of SCI and the breakdown of metabolic homeostasis, thereby facilitating the design of translational research and clinical trials aimed at normalizing WAT function by manipulating sensory nerve endings after injury to the adult spinal cord.

Limitations of the study

Our study indicates that maladaptive changes in sensory processing actively play a role in the deterioration of eWAT function after SCI, thereby contributing to ectopic lipid deposition in non-adipose tissues like the liver. However, we must acknowledge some limitations of our study. To study sensory-dependent structural changes in eWAT, our experimental model of T12 SCI completely transects sensory axons on one side without interrupting sympathetic outflow or impacting sympathetic nerve activity. Whether higher thoracic (e.g., T1–3) SCI that interrupts sympathetic innervation to eWAT more severely impacts eWAT homeostasis remains to be tested. Our three-dimensional imaging of the sensory nerve terminals originating from L3–5 DRG that innervate eWAT indicates these axons are rather sparse and not so densely distributed across the tissue. We found a similar topographic distribution of axonal projections in the eWAT of Nav1.8Cre/Ai9 (RCL-tdTomato) mice. Whether sensory nerve terminals use volume transmission to release CGRP into eWAT rather than point-to-point communication, as is the case in the dorsal horns of the spinal cord, is not known. Additional work will be required to determine whether volume transmission enables sensory nerve terminals to gain control over a large tissue like eWAT that can undergo remarkable size changes under specific developmental, disease, and injury conditions. We identified increased α2δ1 expression in CGRP-positive DRG neurons located below the site of injury after SCI. The transcriptional and post-transcriptional mechanisms underlying changes in α2δ1 expression after SCI are not known and deserve attention for future investigations. Although our data indicate CGRP directly acts on eWAT adipocytes, eWAT stromal cells, including contractile mural cells of blood microvessels, also express the CGRP receptor RAMP1. Thus far, it is not known whether changes in the behavior of mural cells may contribute to eWAT dysfunction and hemodynamic changes after SCI. Additional studies will be needed to determine whether forcing α2δ1 expression in CGRP-positive DRG neurons may be sufficient to drive eWAT lipolysis in the absence of SCI. We discovered profound changes in the presence of immune cells within eWAT depots after SCI. However, it remains to be determined which inflammatory component may be required to drive eWAT dysfunction after SCI. Since chronic inflammation contributes to WAT dysfunction in obesity and diabetes, further research is needed to address this issue. Our results indicate

that GBP administration normalizes eWAT function after SCI. Yet, clinical studies will be required to determine whether normalization of eWAT function through GBP administration translates to SCI individuals.

STAR★METHODS

Detailed methods are provided in the online version of this paper and include the following:

- KEY RESOURCES TABLE
- RESOURCE AVAILABILITY
  - Lead contact
  - Materials availability
  - Data and code availability
- EXPERIMENTAL MODEL AND STUDY PARTICIPANT DETAILS
  - Mice
  - DRG neuron culture
  - Primary adipocyte culture
- METHOD DETAILS
  - Spinal cord injury
  - Histology and immunohistochemistry
  - Ex-vivo lipolysis
  - Immunoblotting
  - Circulating catecholamines, glycerol and free fatty acids in the serum
  - AAV injection and transduction of DRG neurons *in vivo*
  - Fluoro-Gold retrograde tracing
  - DRG neuron culture
  - Primary adipocyte culture and calcium imaging
  - Laser speckle imaging
  - Vasculature tracing, 3D imaging and reconstruction
  - Flow cytometry
  - RNA Isolation and real-time PCR
  - $\alpha 2\delta 1$ knockdown efficiency
  - CGRP levels in eWAT and serum
  - EchoMRI
  - Oil red O staining
  - Insulin and glucose tolerance test
  - Pancreas histology, amylase and lipase activity
  - Indirect calorimetry
  - Prediction of protein-protein interaction network
- QUANTIFICATION AND STATISTICAL ANALYSIS

SUPPLEMENTAL INFORMATION

Supplemental information can be found online at https://doi.org/10.1016/j.xcrm.2024.101525.

ACKNOWLEDGMENTS

We want to thank Drs. Michele Curcio and Ilaria Palmisano for critical reading of the manuscript, Dr. Anna Bratasz (Small Animal Imaging Core, Davis Heart and Lung Research Institute, The Ohio State University) for training on the echoMRI, Lisa Baer (CLAMS Core, Davis Heart and Lung Research Institute, The Ohio State University) for CLAMS analysis, Julia Myers and Dharti Shantaram for technical assistance, and all members of the laboratory for discussion. This work was supported by the National Institute of Neurological Disorders and Stroke (R01NS110681, R01NS124714) and the Chronic Brain Injury program at The Ohio State University, with additional support provided by NIH grant P30CA016058.

AUTHOR CONTRIBUTIONS

D.R. and A.T. conceived the project and designed research; D.R., E.D., J.A.S., S.R.L., A.S., W.S., and A.T. performed research and analyzed the data; J.P. performed statistical analysis; K.T. shared expertise and reagents/laboratory equipment necessary to complete the work; A.T. supervised the research and wrote the paper. All authors provided feedback and contributed to editing the manuscript.

DECLARATION OF INTERESTS

The authors declare that they have no competing financial interests.

Received: July 8, 2023
Revised: January 13, 2024
Accepted: April 2, 2024
Published: April 24, 2024

REFERENCES

1. Garshick, E., Kelley, A., Cohen, S.A., Garrison, A., Tun, C.G., Gagnon, D., and Brown, R. (2005). A prospective assessment of mortality in chronic spinal cord injury. Spinal Cord *43*, 408–416. https://doi.org/10.1038/sj.sc.3101729.
2. Gorgey, A.S., and Gater, D.R., Jr. (2007). Prevalence of Obesity After Spinal Cord Injury. Top. Spinal Cord Inj. Rehabil. *12*, 1–7. https://doi.org/10.1310/sci1204-1.
3. Gorgey, A.S., Wells, K.M., and Austin, T.L. (2015). Adiposity and spinal cord injury. World J. Orthop. *6*, 567–576. https://doi.org/10.5312/wjo.v6.i8.567.
4. Goodus, M.T., Carson, K.E., Sauerbeck, A.D., Dey, P., Alfredo, A.N., Popovich, P.G., Bruno, R.S., and McTigue, D.M. (2021). Liver inflammation at the time of spinal cord injury enhances intraspinal pathology, liver injury, metabolic syndrome and locomotor deficits. Exp. Neurol. *342*, 113725. https://doi.org/10.1016/j.expneurol.2021.113725.
5. Jones, L.M., Legge, M., and Goulding, A. (2003). Healthy body mass index values often underestimate body fat in men with spinal cord injury. Arch. Phys. Med. Rehabil. *84*, 1068–1071. https://doi.org/10.1016/s0003-9993(03)00045-5.
6. Modlesky, C.M., Bickel, C.S., Slade, J.M., Meyer, R.A., Cureton, K.J., and Dudley, G.A. (2004). Assessment of skeletal muscle mass in men with spinal cord injury using dual-energy X-ray absorptiometry and magnetic resonance imaging. J. Appl. Physiol. (1985) *96*, 561–565. https://doi.org/10.1152/japplphysiol.00207.2003.
7. Furlan, J.C., and Fehlings, M.G. (2008). Cardiovascular complications after acute spinal cord injury: pathophysiology, diagnosis, and management. Neurosurg. Focus *25*, E13. https://doi.org/10.3171/FOC.2008.25.11.E13.
8. Kahn, C.R., Wang, G., and Lee, K.Y. (2019). Altered adipose tissue and adipocyte function in the pathogenesis of metabolic syndrome. J. Clin. Invest. *129*, 3990–4000. https://doi.org/10.1172/JCI129187.
9. Lass, A., Zimmermann, R., Oberer, M., and Zechner, R. (2011). Lipolysis - a highly regulated multi-enzyme complex mediates the catabolism of cellular fat stores. Prog. Lipid Res. *50*, 14–27. https://doi.org/10.1016/j.plipres.2010.10.004.
10. Schweiger, M., Schreiber, R., Haemmerle, G., Lass, A., Fledelius, C., Jacobsen, P., Tornqvist, H., Zechner, R., and Zimmermann, R. (2006). Adipose triglyceride lipase and hormone-sensitive lipase are the major enzymes in adipose tissue triacylglycerol catabolism. J. Biol. Chem. *281*, 40236–40241. https://doi.org/10.1074/jbc.M608048200.
11. Bartness, T.J., Shrestha, Y.B., Vaughan, C.H., Schwartz, G.J., and Song, C.K. (2010). Sensory and sympathetic nervous system control of white adipose tissue lipolysis. Mol. Cell. Endocrinol. *318*, 34–43. https://doi.org/10.1016/j.mce.2009.08.031.
12. Bamshad, M., Aoki, V.T., Adkison, M.G., Warren, W.S., and Bartness, T.J. (1998). Central nervous system origins of the sympathetic nervous system outflow to white adipose tissue. Am. J. Physiol. *275*, R291–R299. https://doi.org/10.1152/ajpregu.1998.275.1.R291.

13. Bowers, R.R., Festuccia, W.T.L., Song, C.K., Shi, H., Migliorini, R.H., and Bartness, T.J. (2004). Sympathetic innervation of white adipose tissue and its regulation of fat cell number. Am. J. Physiol. Regul. Integr. Comp. Physiol. *286*, R1167–R1175. https://doi.org/10.1152/ajpregu.00558.2003.

14. Foster, M.T., and Bartness, T.J. (2006). Sympathetic but not sensory denervation stimulates white adipocyte proliferation. Am. J. Physiol. Regul. Integr. Comp. Physiol. *291*, R1630–R1637. https://doi.org/10.1152/ajpregu.00197.2006.

15. Shi, H., Song, C.K., Giordano, A., Cinti, S., and Bartness, T.J. (2005). Sensory or sympathetic white adipose tissue denervation differentially affects depot growth and cellularity. Am. J. Physiol. Regul. Integr. Comp. Physiol. *288*, R1028–R1037. https://doi.org/10.1152/ajpregu.00648.2004.

16. Brennan, F.H., Noble, B.T., Wang, Y., Guan, Z., Davis, H., Mo, X., Harris, C., Eroglu, C., Ferguson, A.R., and Popovich, P.G. (2021). Acute post-injury blockade of alpha2delta-1 calcium channel subunits prevents pathological autonomic plasticity after spinal cord injury. Cell Rep. *34*, 108667. https://doi.org/10.1016/j.celrep.2020.108667.

17. Dahimene, S., von Elsner, L., Holling, T., Mattas, L.S., Pickard, J., Lessel, D., Pilch, K.S., Kadurin, I., Pratt, W.S., Zhulin, I.B., et al. (2022). Biallelic CACNA2D1 loss-of-function variants cause early-onset developmental epileptic encephalopathy. Brain *145*, 2721–2729. https://doi.org/10.1093/brain/awac081.

18. Li, H., Graber, K.D., Jin, S., McDonald, W., Barres, B.A., and Prince, D.A. (2012). Gabapentin decreases epileptiform discharges in a chronic model of neocortical trauma. Neurobiol. Dis. *48*, 429–438. https://doi.org/10.1016/j.nbd.2012.06.019.

19. Sun, W., Larson, M.J., Kiyoshi, C.M., Annett, A.J., Stalker, W.A., Peng, J., and Tedeschi, A. (2020). Gabapentinoid treatment promotes corticospinal plasticity and regeneration following murine spinal cord injury. J. Clin. Invest. *130*, 345–358. https://doi.org/10.1172/JCI130391.

20. Tedeschi, A., Dupraz, S., Laskowski, C.J., Xue, J., Ulas, T., Beyer, M., Schultze, J.L., and Bradke, F. (2016). The Calcium Channel Subunit Alpha2delta2 Suppresses Axon Regeneration in the Adult CNS. Neuron *92*, 419–434. https://doi.org/10.1016/j.neuron.2016.09.026.

21. Tedeschi, A., Larson, M.J.E., Zouridakis, A., Mo, L., Bordbar, A., Myers, J.M., Qin, H.Y., Rodocker, H.I., Fan, F., Lannutti, J.J., et al. (2022). Harnessing cortical plasticity via gabapentinoid administration promotes recovery after stroke. Brain *145*, 2378–2393. https://doi.org/10.1093/brain/awac103.

22. Hoppa, M.B., Lana, B., Margas, W., Dolphin, A.C., and Ryan, T.A. (2012). alpha2delta expression sets presynaptic calcium channel abundance and release probability. Nature *486*, 122–125. https://doi.org/10.1038/nature11033.

23. Li, C.Y., Zhang, X.L., Matthews, E.A., Li, K.W., Kurwa, A., Boroujerdi, A., Gross, J., Gold, M.S., Dickenson, A.H., Feng, G., and Luo, Z.D. (2006). Calcium channel alpha2delta1 subunit mediates spinal hyperexcitability in pain modulation. Pain *125*, 20–34. https://doi.org/10.1016/j.pain.2006.04.022.

24. Luo, Z.D., Calcutt, N.A., Higuera, E.S., Valder, C.R., Song, Y.H., Svensson, C.I., and Myers, R.R. (2002). Injury type-specific calcium channel alpha 2 delta-1 subunit up-regulation in rat neuropathic pain models correlates with antiallodynic effects of gabapentin. J. Pharmacol. Exp. Ther. *303*, 1199–1205. https://doi.org/10.1124/jpet.102.041574.

25. Luo, Z.D., Chaplan, S.R., Higuera, E.S., Sorkin, L.S., Stauderman, K.A., Williams, M.E., and Yaksh, T.L. (2001). Upregulation of dorsal root ganglion (alpha)2(delta) calcium channel subunit and its correlation with allodynia in spinal nerve-injured rats. J. Neurosci. *21*, 1868–1875. https://doi.org/10.1523/JNEUROSCI.21-06-01868.2001.

26. Li, C.Y., Song, Y.H., Higuera, E.S., and Luo, Z.D. (2004). Spinal dorsal horn calcium channel alpha2delta-1 subunit upregulation contributes to peripheral nerve injury-induced tactile allodynia. J. Neurosci. *24*, 8494–8499. https://doi.org/10.1523/JNEUROSCI.2982-04.2004.

27. Faria, L.C., Gu, F., Parada, I., Barres, B., Luo, Z.D., and Prince, D.A. (2017). Epileptiform activity and behavioral arrests in mice overexpressing the calcium channel subunit alpha2delta-1. Neurobiol. Dis. *102*, 70–80. https://doi.org/10.1016/j.nbd.2017.01.009.

28. Lau, L.A., Noubary, F., Wang, D., and Dulla, C.G. (2017). alpha2delta-1 Signaling Drives Cell Death, Synaptogenesis, Circuit Reorganization, and Gabapentin-Mediated Neuroprotection in a Model of Insult-Induced Cortical Malformation. eNeuro *4*, ENEURO.0316-17.2017. https://doi.org/10.1523/ENEURO.0316-17.2017.

29. Prüss, H., Tedeschi, A., Thiriot, A., Lynch, L., Loughhead, S.M., Stutte, S., Mazo, I.B., Kopp, M.A., Brommer, B., Blex, C., et al. (2017). Spinal cord injury-induced immunodeficiency is mediated by a sympathetic-neuroendocrine adrenal reflex. Nat. Neurosci. *20*, 1549–1559. https://doi.org/10.1038/nn.4643.

30. Grabner, G.F., Xie, H., Schweiger, M., and Zechner, R. (2021). Lipolysis: cellular mechanisms for lipid mobilization from fat stores. Nat. Metab. *3*, 1445–1465. https://doi.org/10.1038/s42255-021-00493-6.

31. Brasaemle, D.L., Levin, D.M., Adler-Wailes, D.C., and Londos, C. (2000). The lipolytic stimulation of 3T3-L1 adipocytes promotes the translocation of hormone-sensitive lipase to the surfaces of lipid storage droplets. Biochim. Biophys. Acta *1483*, 251–262. https://doi.org/10.1016/s1388-1981(99)00179-1.

32. Wang, Y., Leung, V.H., Zhang, Y., Nudell, V.S., Loud, M., Servin-Vences, M.R., Yang, D., Wang, K., Moya-Garzon, M.D., Li, V.L., et al. (2022). The role of somatosensory innervation of adipose tissues. Nature *609*, 569–574. https://doi.org/10.1038/s41586-022-05137-7.

33. Willows, J.W., Blaszkiewicz, M., Lamore, A., Borer, S., Dubois, A.L., Garner, E., Breeding, W.P., Tilbury, K.B., Khalil, A., and Townsend, K.L. (2021). Visualization and analysis of whole depot adipose tissue neural innervation. iScience *24*, 103127. https://doi.org/10.1016/j.isci.2021.103127.

34. Bauer, C.S., Nieto-Rostro, M., Rahman, W., Tran-Van-Minh, A., Ferron, L., Douglas, L., Kadurin, I., Sri Ranjan, Y., Fernandez-Alacid, L., Millar, N.S., et al. (2009). The increased trafficking of the calcium channel subunit alpha2delta-1 to presynaptic terminals in neuropathic pain is inhibited by the alpha2delta ligand pregabalin. J. Neurosci. *29*, 4076–4088. https://doi.org/10.1523/JNEUROSCI.0356-09.2009.

35. Bikbaev, A., Ciuraszkiewicz-Wojciech, A., Heck, J., Klatt, O., Freund, R., Mitlöhner, J., Enrile Lacalle, S., Sun, M., Repetto, D., Frischknecht, R., et al. (2020). Auxiliary alpha2delta1 and alpha2delta3 Subunits of Calcium Channels Drive Excitatory and Inhibitory Neuronal Network Development. J. Neurosci. *40*, 4824–4841. https://doi.org/10.1523/JNEUROSCI.1707-19.2020.

36. Boroujerdi, A., Kim, H.K., Lyu, Y.S., Kim, D.S., Figueroa, K.W., Chung, J.M., and Luo, D.Z. (2008). Injury discharges regulate calcium channel alpha-2-delta-1 subunit upregulation in the dorsal horn that contributes to initiation of neuropathic pain. Pain *139*, 358–366. https://doi.org/10.1016/j.pain.2008.05.004.

37. Hessenberger, M., Haddad, S., and Obermair, G.J. (2023). Pathophysiological Roles of Auxiliary Calcium Channel alpha(2)delta Subunits. Handb. Exp. Pharmacol. *279*, 289–316. https://doi.org/10.1007/164_2022_630.

38. Chiu, I.M., Barrett, L.B., Williams, E.K., Strochlic, D.E., Lee, S., Weyer, A.D., Lou, S., Bryman, G.S., Roberson, D.P., Ghasemlou, N., et al. (2014). Transcriptional profiling at whole population and single cell levels reveals somatosensory neuron molecular diversity. Elife *3*, e04660. https://doi.org/10.7554/eLife.04660.

39. Nieto-Rostro, M., Ramgoolam, K., Pratt, W.S., Kulik, A., and Dolphin, A.C. (2018). Ablation of alpha(2)delta-1 inhibits cell-surface trafficking of endogenous N-type calcium channels in the pain pathway in vivo. Proc. Natl. Acad. Sci. USA *115*, E12043–E12052. https://doi.org/10.1073/pnas.1811212115.

40. Nguyen, D., Deng, P., Matthews, E.A., Kim, D.S., Feng, G., Dickenson, A.H., Xu, Z.C., and Luo, Z.D. (2009). Enhanced pre-synaptic glutamate release in deep-dorsal horn contributes to calcium channel alpha-2-delta-1 protein-mediated spinal sensitization and behavioral hypersensitivity. Mol. Pain *5*, 6. https://doi.org/10.1186/1744-8069-5-6.

41. Newton, R.A., Bingham, S., Case, P.C., Sanger, G.J., and Lawson, S.N. (2001). Dorsal root ganglion neurons show increased expression of the calcium channel alpha2delta-1 subunit following partial sciatic nerve injury. Brain Res. Mol. Brain Res. *95*, 1–8. https://doi.org/10.1016/s0169-328x(01)00188-7.

42. Catterall, W.A. (2011). Voltage-gated calcium channels. Cold Spring Harb. Perspect. Biol. *3*, a003947. https://doi.org/10.1101/cshperspect.a003947.

43. Nieto-Rostro, M., Patel, R., Dickenson, A.H., and Dolphin, A.C. (2023). Nerve injury increases native Ca V 2.2 trafficking in dorsal root ganglion mechanoreceptors. Pain *164*, 1264–1279. https://doi.org/10.1097/j.pain.0000000000002846.

44. Aveseh, M., Koushkie-Jahromi, M., Nemati, J., and Esmaeili-Mahani, S. (2018). Serum calcitonin gene-related peptide facilitates adipose tissue lipolysis during exercise via PIPLC/IP3 pathways. Endocrine *61*, 462–472. https://doi.org/10.1007/s12020-018-1640-2.

45. Zemel, M.B., Shi, H., Greer, B., Dirienzo, D., and Zemel, P.C. (2000). Regulation of adiposity by dietary calcium. FASEB J *14*, 1132–1138.

46. Brain, S.D., Williams, T.J., Tippins, J.R., Morris, H.R., and MacIntyre, I. (1985). Calcitonin gene-related peptide is a potent vasodilator. Nature *313*, 54–56. https://doi.org/10.1038/313054a0.

47. Lino Rodrigues, K., Vieira Dias Da Silva, V., Nunes Goulart da Silva Pereira, E., Rangel Silvares, R., Peres de Araujo, B., Eduardo Ilaquita Flores, E., Ramos, I.P., Pereira Borges, J., Fernandes-Santos, C., and Daliry, A. (2022). Aerobic Exercise Training Improves Microvascular Function and Oxidative Stress Parameters in Diet-Induced Type 2 Diabetic Mice. Diabetes Metab. Syndr. Obes. *15*, 2991–3005. https://doi.org/10.2147/DMSO.S365496.

48. Rutkowski, J.M., Davis, K.E., and Scherer, P.E. (2009). Mechanisms of obesity and related pathologies: the macro- and microcirculation of adipose tissue. FEBS J. *276*, 5738–5746. https://doi.org/10.1111/j.1742-4658.2009.07303.x.

49. Boesch, M., Lindhorst, A., Feio-Azevedo, R., Brescia, P., Silvestri, A., Lannoo, M., Deleus, E., Jaekers, J., Topal, H., Topal, B., et al. (2024). Adipose tissue macrophage dysfunction is associated with a breach of vascular integrity in NASH. J. Hepatol. *80*, 397–408. https://doi.org/10.1016/j.jhep.2023.10.039.

50. Benemei, S., Nicoletti, P., Capone, J.G., and Geppetti, P. (2009). CGRP receptors in the control of pain and inflammation. Curr. Opin. Pharmacol. *9*, 9–14. https://doi.org/10.1016/j.coph.2008.12.007.

51. Xu, H., Barnes, G.T., Yang, Q., Tan, G., Yang, D., Chou, C.J., Sole, J., Nichols, A., Ross, J.S., Tartaglia, L.A., and Chen, H. (2003). Chronic inflammation in fat plays a crucial role in the development of obesity-related insulin resistance. J. Clin. Invest. *112*, 1821–1830. https://doi.org/10.1172/JCI19451.

52. Park, J., Yu, Y.P., Zhou, C.Y., Li, K.W., Wang, D., Chang, E., Kim, D.S., Vo, B., Zhang, X., Gong, N., et al. (2016). Central Mechanisms Mediating Thrombospondin-4-induced Pain States. J. Biol. Chem. *291*, 13335–13348. https://doi.org/10.1074/jbc.M116.723478.

53. Stirling, L.C., Forlani, G., Baker, M.D., Wood, J.N., Matthews, E.A., Dickenson, A.H., and Nassar, M.A. (2005). Nociceptor-specific gene deletion using heterozygous NaV1.8-Cre recombinase mice. Pain *113*, 27–36. https://doi.org/10.1016/j.pain.2004.08.015.

54. Shields, S.D., Ahn, H.S., Yang, Y., Han, C., Seal, R.P., Wood, J.N., Waxman, S.G., and Dib-Hajj, S.D. (2012). Nav1.8 expression is not restricted to nociceptors in mouse peripheral nervous system. Pain *153*, 2017–2030. https://doi.org/10.1016/j.pain.2012.04.022.

55. Gee, N.S., Brown, J.P., Dissanayake, V.U., Offord, J., Thurlow, R., and Woodruff, G.N. (1996). The novel anticonvulsant drug, gabapentin (Neurontin), binds to the alpha2delta subunit of a calcium channel. J. Biol. Chem. *271*, 5768–5776. https://doi.org/10.1074/jbc.271.10.5768.

56. Gong, H.C., Hang, J., Kohler, W., Li, L., and Su, T.Z. (2001). Tissue-specific expression and gabapentin-binding properties of calcium channel alpha2-delta subunit subtypes. J. Membr. Biol. *184*, 35–43. https://doi.org/10.1007/s00232-001-0072-7.

57. Powell, D., Affuso, O., and Chen, Y. (2017). Weight change after spinal cord injury. J. Spinal Cord Med. *40*, 130–137. https://doi.org/10.1179/2045772314Y.0000000264.

58. Bays, H.E., Toth, P.P., Kris-Etherton, P.M., Abate, N., Aronne, L.J., Brown, W.V., Gonzalez-Campoy, J.M., Jones, S.R., Kumar, R., La Forge, R., and Samuel, V.T. (2013). Obesity, adiposity, and dyslipidemia: a consensus statement from the National Lipid Association. J. Clin. Lipidol. *7*, 304–383. https://doi.org/10.1016/j.jacl.2013.04.001.

59. Cox, S.A., Weiss, S.M., Posuniak, E.A., Worthington, P., Prioleau, M., and Heffley, G. (1985). Energy expenditure after spinal cord injury: an evaluation of stable rehabilitating patients. J. Trauma *25*, 419–423.

60. Felsted, J.A., Chien, C.H., Wang, D., Panessiti, M., Ameroso, D., Greenberg, A., Feng, G., Kong, D., and Rios, M. (2017). Alpha2delta-1 in SF1(+) Neurons of the Ventromedial Hypothalamus Is an Essential Regulator of Glucose and Lipid Homeostasis. Cell Rep. *21*, 2737–2747. https://doi.org/10.1016/j.celrep.2017.11.048.

61. Mastrolia, V., Flucher, S.M., Obermair, G.J., Drach, M., Hofer, H., Renström, E., Schwartz, A., Striessnig, J., Flucher, B.E., and Tuluc, P. (2017). Loss of alpha(2)delta-1 Calcium Channel Subunit Function Increases the Susceptibility for Diabetes. Diabetes *66*, 897–907. https://doi.org/10.2337/db16-0336.

62. Latifi, S., Koushki, D., Norouzi Javidan, A., Matin, M., and Sabour, H. (2013). Changes of leptin concentration in plasma in patients with spinal cord injury: a meta-analysis. Spinal Cord *51*, 728–731. https://doi.org/10.1038/sc.2013.82.

63. Polyzos, S.A., Aronis, K.N., Kountouras, J., Raptis, D.D., Vasiloglou, M.F., and Mantzoros, C.S. (2016). Circulating leptin in non-alcoholic fatty liver disease: a systematic review and meta-analysis. Diabetologia *59*, 30–43. https://doi.org/10.1007/s00125-015-3769-3.

64. Ferré, P., and Foufelle, F. (2007). SREBP-1c transcription factor and lipid homeostasis: clinical perspective. Horm. Res. *68*, 72–82. https://doi.org/10.1159/000100426.

65. Shimomura, I., Bashmakov, Y., and Horton, J.D. (1999). Increased levels of nuclear SREBP-1c associated with fatty livers in two mouse models of diabetes mellitus. J. Biol. Chem. *274*, 30028–30032. https://doi.org/10.1074/jbc.274.42.30028.

66. Shimomura, I., Bashmakov, Y., Ikemoto, S., Horton, J.D., Brown, M.S., and Goldstein, J.L. (1999). Insulin selectively increases SREBP-1c mRNA in the livers of rats with streptozotocin-induced diabetes. Proc. Natl. Acad. Sci. USA *96*, 13656–13661. https://doi.org/10.1073/pnas.96.24.13656.

67. Shimomura, I., Hammer, R.E., Richardson, J.A., Ikemoto, S., Bashmakov, Y., Goldstein, J.L., and Brown, M.S. (1998). Insulin resistance and diabetes mellitus in transgenic mice expressing nuclear SREBP-1c in adipose tissue: model for congenital generalized lipodystrophy. Genes Dev. *12*, 3182–3194. https://doi.org/10.1101/gad.12.20.3182.

68. Fhu, C.W., and Ali, A. (2020). Fatty Acid Synthase: An Emerging Target in Cancer. Molecules *25*, 3935. https://doi.org/10.3390/molecules25173935.

69. Dorn, C., Riener, M.O., Kirovski, G., Saugspier, M., Steib, K., Weiss, T.S., Gäbele, E., Kristiansen, G., Hartmann, A., and Hellerbrand, C. (2010). Expression of fatty acid synthase in nonalcoholic fatty liver disease. Int. J. Clin. Exp. Pathol. *3*, 505–514.

70. Chait, A., and den Hartigh, L.J. (2020). Adipose Tissue Distribution, Inflammation and Its Metabolic Consequences, Including Diabetes and Cardiovascular Disease. Front. Cardiovasc. Med. *7*, 22. https://doi.org/10.3389/fcvm.2020.00022.

71. Haemmerle, G., Lass, A., Zimmermann, R., Gorkiewicz, G., Meyer, C., Rozman, J., Heldmaier, G., Maier, R., Theussl, C., Eder, S., et al. (2006). Defective lipolysis and altered energy metabolism in mice lacking adipose triglyceride lipase. Science *312*, 734–737. https://doi.org/10.1126/science.1123965.

72. Rohm, T.V., Meier, D.T., Olefsky, J.M., and Donath, M.Y. (2022). Inflammation in obesity, diabetes, and related disorders. Immunity *55*, 31–55. https://doi.org/10.1016/j.immuni.2021.12.013.

73. Vidman, S., Dion, E., and Tedeschi, A. (2024). A versatile pipeline for high-fidelity imaging and analysis of vascular networks across the body. Bio-protocol *14*, e4938. https://doi.org/10.21769/BioProtoc.4938.

74. Farkas, G.J., Gorgey, A.S., Dolbow, D.R., Berg, A.S., and Gater, D.R. (2018). The influence of level of spinal cord injury on adipose tissue and its relationship to inflammatory adipokines and cardiometabolic profiles. J. Spinal Cord Med. *41*, 407–415. https://doi.org/10.1080/10790268.2017.1357918.

75. Shi, C., and Pamer, E.G. (2011). Monocyte recruitment during infection and inflammation. Nat. Rev. Immunol. *11*, 762–774. https://doi.org/10.1038/nri3070.

76. Wang, D., Tai, P.W.L., and Gao, G. (2019). Adeno-associated virus vector as a platform for gene therapy delivery. Nat. Rev. Drug Discov. *18*, 358–378. https://doi.org/10.1038/s41573-019-0012-9.

77. Paige, C., Plasencia-Fernandez, I., Kume, M., Papalampropoulou-Tsiridou, M., Lorenzo, L.E., David, E.T., He, L., Mejia, G.L., Driskill, C., Ferrini, F., et al. (2022). A Female-Specific Role for Calcitonin Gene-Related Peptide (CGRP) in Rodent Pain Models. J. Neurosci. *42*, 1930–1944. https://doi.org/10.1523/JNEUROSCI.1137-21.2022.

78. Nair, A.B., and Jacob, S. (2016). A simple practice guide for dose conversion between animals and human. J. Basic Clin. Pharm. *7*, 27–31. https://doi.org/10.4103/0976-0105.177703.

79. Levendoglu, F., Ogün, C.O., Ozerbil, O., Ogün, T.C., and Ugurlu, H. (2004). Gabapentin is a first line drug for the treatment of neuropathic pain in spinal cord injury. Spine *29*, 743–751. https://doi.org/10.1097/01.brs.0000112068.16108.3a.

80. Toth, C. (2014). Pregabalin: latest safety evidence and clinical implications for the management of neuropathic pain. Ther. Adv. Drug Saf. *5*, 38–56. https://doi.org/10.1177/2042098613505614.

81. Warner, F.M., Cragg, J.J., Jutzeler, C.R., Röhrich, F., Weidner, N., Saur, M., Maier, D.D., Schuld, C., EMSCI Sites; Curt, A., and Kramer, J.K. (2017). Early Administration of Gabapentinoids Improves Motor Recovery after Human Spinal Cord Injury. Cell Rep. *18*, 1614–1618. https://doi.org/10.1016/j.celrep.2017.01.048.

82. Wilson, J.R., Doty, S., Petitt, J.C., El-Abtah, M., Francis, J.J., Sharpe, M.G., Kelly, M.L., and Anderson, K.D. (2022). Feasibility of gabapentin as an intervention for neurorecovery after an acute spinal cord injury: Protocol. Front. Neurol. *13*, 1033386. https://doi.org/10.3389/fneur.2022.1033386.

83. Jutzeler, C.R., Bourguignon, L., Tong, B., Ronca, E., Bailey, E., Harel, N.Y., Geisler, F., Ferguson, A.R., Kwon, B.K., Cragg, J.J., et al. (2023). Pharmacological management of acute spinal cord injury: a longitudinal multicohort observational study. Sci. Rep. *13*, 5434. https://doi.org/10.1038/s41598-023-31773-8.

84. Madisen, L., Zwingman, T.A., Sunkin, S.M., Oh, S.W., Zariwala, H.A., Gu, H., Ng, L.L., Palmiter, R.D., Hawrylycz, M.J., Jones, A.R., et al. (2010). A robust and high-throughput Cre reporting and characterization system for the whole mouse brain. Nat. Neurosci. *13*, 133–140. https://doi.org/10.1038/nn.2467.

85. Nassar, M.A., Stirling, L.C., Forlani, G., Baker, M.D., Matthews, E.A., Dickenson, A.H., and Wood, J.N. (2004). Nociceptor-specific gene deletion reveals a major role for Nav1.7 (PN1) in acute and inflammatory pain. Proc. Natl. Acad. Sci. USA *101*, 12706–12711. https://doi.org/10.1073/pnas.0404915101.

86. Zaqout, S., Becker, L.L., and Kaindl, A.M. (2020). Immunofluorescence Staining of Paraffin Sections Step by Step. Front. Neuroanat. *14*, 582218. https://doi.org/10.3389/fnana.2020.582218.

87. Roy, D., Myers, J.M., and Tedeschi, A. (2022). Protocol for assessing ex vivo lipolysis of murine adipose tissue. STAR Protoc. *3*, 101518. https://doi.org/10.1016/j.xpro.2022.101518.

88. Rodbell, M. (1964). Localization of Lipoprotein Lipase in Fat Cells of Rat Adipose Tissue. J. Biol. Chem. *239*, 753–755.

89. Susaki, E.A., Tainaka, K., Perrin, D., Yukinaga, H., Kuno, A., and Ueda, H.R. (2015). Advanced CUBIC protocols for whole-brain and whole-body clearing and imaging. Nat. Protoc. *10*, 1709–1727. https://doi.org/10.1038/nprot.2015.085.

90. Sas, A.R., Carbajal, K.S., Jerome, A.D., Menon, R., Yoon, C., Kalinski, A.L., Giger, R.J., and Segal, B.M. (2020). A new neutrophil subset promotes CNS neuron survival and axon regeneration. Nat. Immunol. *21*, 1496–1505. https://doi.org/10.1038/s41590-020-00813-0.

91. Mehlem, A., Hagberg, C.E., Muhl, L., Eriksson, U., and Falkevall, A. (2013). Imaging of neutral lipids by oil red O for analyzing the metabolic status in health and disease. Nat. Protoc. *8*, 1149–1154. https://doi.org/10.1038/nprot.2013.055.

92. Szklarczyk, D., Kirsch, R., Koutrouli, M., Nastou, K., Mehryary, F., Hachilif, R., Gable, A.L., Fang, T., Doncheva, N.T., Pyysalo, S., et al. (2023). The STRING database in 2023: protein-protein association networks and functional enrichment analyses for any sequenced genome of interest. Nucleic Acids Res. *51*, D638–D646. https://doi.org/10.1093/nar/gkac1000.

93. Shannon, P., Markiel, A., Ozier, O., Baliga, N.S., Wang, J.T., Ramage, D., Amin, N., Schwikowski, B., and Ideker, T. (2003). Cytoscape: a software environment for integrated models of biomolecular interaction networks. Genome Res. *13*, 2498–2504. https://doi.org/10.1101/gr.1239303.

STAR★METHODS

KEY RESOURCES TABLE

REAGENT or RESOURCE	SOURCE	IDENTIFIER
Antibodies		
Rabbit Phospho-HSL (Ser660), 1:1000 (WB) and 1:500 (IHC)	Cell Signaling Technology	Cat #45804; RRID: AB_2893315
Rabbit HSL, 1:1000 (WB)	Cell Signaling Technology	Cat #4107; RRID: AB_2296900
Rabbit ATGL (30A4) mAb, 1:1000 (WB) and 1:500 (IHC)	Cell Signaling Technology	Cat #2439; RRID: AB_2167953
Rabbit GAPDH (14C10) mAb, 1:5000 (WB)	Cell Signaling Technology	Cat #2118; RRID: AB_561053
Rabbit Perilipin-1 (D1D8) XP® mAb, 1:2000 (IHC)	Cell Signaling Technology	Cat #9349; RRID: AB_10829911
Rabbit $\alpha 2\delta 1$ polyAb, 1:500 (IHC)	Sigma	Cat #C5105; RRID: AB_258885
Rabbit CGRP polyAb, 1:600 (IHC)	Sigma	Cat #C8198; RRID: AB_259091
Mouse CGRP mAb, 1:100 (IHC)	Abcam	Cat #AB81887-1001; RRID: AB_1658411
Rabbit Cav2.1 polyAb, 1:200 (IHC)	Alomone Labs	Cat #ACC-001; RRID: AB_2039764
Rabbit RAMP-1 polyAb, 1:1000 (WB) and 1:100 (IHC)	Invitrogen	Cat # PA5-110265; RRID: AB_2855676
Goat anti-rabbit IgG Fc, cross-adsorbed secondary antibody, Alexa Fluor™ 555, 1:400 (IHC)	Thermo Fisher Scientific	Cat # A78954; RRID: AB_2535849
Goat anti-rabbit IgG (H + L), cross-adsorbed secondary antibody, Alexa Fluor™ 488, 1:400 (IHC)	Thermo Fisher Scientific	Cat # A-11008; RRID: AB_143165
Anti-rabbit IgG, HRP-linked, 1:3000 (WB)	Cell Signaling Technology	Cat #7074; RRID: AB_2099233
Donkey anti-rabbit IgG, HRP conjugate, 1:10000 (WB)	Sigma-Aldrich	Cat #AP182P; RRID: AB_92591
CD16/32, 2.4G2, 1:200 (flow cytometry)	eBiosciences	Cat #14-0161
CD45, BUV805, 30-F11, 1:100 (flow cytometry)	BD Biosciences	Cat #752415; RRID:AB_2917429
Ly6G, BUV563, 1A8, 1:50 (flow cytometry)	BD Biosciences	Cat #612921; RRID:AB_2870206
CD11b, BV786, M1/70, 1:500 (flow cytometry)	BD Biosciences	Cat #740861; RRID:AB_2740514
F4/80, PE, T45-2342, 1:100 (flow cytometry)	BD Biosciences	Cat #565410; RRID:AB_2687527
CD11c, BUV737, HL3, 1:100 (flow cytometry)	BD Biosciences	Cat #612797; RRID:AB_2870124
CD14, BV650, rmC5-3, 1:100 (flow cytometry)	BD Biosciences	Cat #740486; RRID:AB_2740209
CD115, BUV395, T38-320, 1:100 (flow cytometry)	BD Biosciences	Cat #743642; RRID:AB_2741652
I-A/I-E, BUV496, M5, 114.15.2, 1:100 (flow cytometry)	BD Biosciences	Cat #750281; RRID:AB_2874472
CD64, APC, X54-5/7.1, 1:100 (flow cytometry)	BD Biosciences	Cat #558539; RRID:AB_647120
MerTK, PE-Cy7, DS5MMER, 1:100 (flow cytometry)	Invitrogen	Cat #25-5751-82; RRID:AB_2573466
Arginase 1, FITC 1:20 (flow cytometry)	R&D Systems	Cat # IC5868F; RRID:AB_10718118
Ly6c, PE-CF594, AL-21, 1:100 (flow cytometry)	BD Biosciences	Cat #562728; RRID:AB_2737749
CD206, Alexa Fluor 700, MR6F3, 1:50 (flow cytometry)	Invitrogen	Cat# 56-2061-82; RRID:AB_276272
Chemicals, peptides, and recombinant proteins		
Paraformaldehyde	Sigma-Aldrich	Cat #158127
Ethyl alcohol	Sigma-Aldrich	Cat #E7023
Xylenes	Thermo Fisher Scientific	Cat #X5-1
Hydrogen peroxide, 30%	Thermo Fisher Scientific	Cat #H325-500
Antigen unmasking solution, citrate-based	Vector Laboratories	Cat #H-3300-250
Triton™X-100	Sigma-Aldrich	Cat #T8787
Phosphate buffered saline, pH 7.4	Thermo Fisher Scientific	Cat #10055154
Bovine serum albumin	Sigma-Aldrich	Cat #A3059
Bovine serum albumin, fatty acid free	Sigma-Aldrich	Cat #A7030
HEPES	Sigma-Aldrich	Cat #H4034
Gibco™ DPBS, no calcium, no magnesium	Thermo Fisher Scientific	Cat #14190144
Gey's balanced salt solution	Sigma-Aldrich	Cat #G9779
Gibco™ DMEM, high glucose, pyruvate	Thermo Fisher Scientific	Cat #11995073

(*Continued on next page*)

Continued

REAGENT or RESOURCE	SOURCE	IDENTIFIER
Gibco™ Neurobasal A medium	Thermo Fisher Scientific	Cat #12349-015
HBSS	Thermo Fisher Scientific	Cat #14175-095
Laminin	Roche	Cat #11243217001
B27 supplement (50X)	Thermo Fisher Scientific	Cat #17504044
Fetal bovine serum	Thermo Fisher Scientific	Cat #26140079
Sodium bicarbonate	Thermo Fisher Scientific	Cat #S233500
Sodium chloride	Thermo Fisher Scientific	Cat #S271-3
Magnesium sulfate	Sigma-Aldrich	Cat #M7506
Calcium chloride	MP Biomedicals	Cat #153502
Potassium phosphate dibasic	Sigma-Aldrich	Cat #P3786
0.9% Sodium chloride	Aqualite System	Cat #0409-7138-09
Insulin (Humulin R)	Thermo Fisher Scientific	Cat #NC1415864
Isoprenaline hydrochloride	Abcam	Cat #ab146724
Gabapentin	Sigma-Aldrich	Cat #PHR1049
Adenosine	Sigma-Aldrich	Cat #A4036
Tris-HCl	Sigma-Aldrich	Cat #10812846001
Sodium deoxycholate	Sigma-Aldrich	Cat #D6750
Np-40 (IGEPAL CA-630)	Thermo Fisher Scientific	Cat #J61055
Sodium dodecyl sulfate (SDS)	Bio-Rad	Cat #1610302
0.5 M Ethelene-di-amine-tetraacetic acid (EDTA)	Thermo Fisher Scientific	Cat #AM9260G
Ponceau S solution	Sigma-Aldrich	Cat #P7170
Blotting grade blocker non-fat dry milk	Bio-Rad	Cat #1706404XTU
cOmplete™, EDTA-free protease inhibitor cocktail	Sigma-Aldrich	Cat #04693132001
PhosSTOP™	Sigma-Aldrich	Cat #4906845001
Collagenase, type 1	Worthington	Cat # LS004194
Calcitonin gene-related peptide rat	Sigma-Aldrich	Cat #C0292
Fluoro-Gold	Fluorochrome, LLC	Cat #Fluoro-Gold 20mg
Cytofix/cytoperm	BD Biosciences	Cat #51-2090KZ
Perm wash	BD Biosciences	Cat #51-2091KZ
Brilliant stain buffer	BD Biosciences	Cat #566349
Fixable viability, eFlour780	eBioscience	Cat #65-0865
Critical commercial assays		
Catecholamines ELISA Kit	Abcam	Cat #ab287795
Hematoxylin and eosin stain kit	Abcam	Cat #ab245880
Glycerol assay kit (cell-based)	Abcam	Cat #ab133130
Free fatty acid quantification kit	Sigma-Aldrich	Cat #MAK044
Mouse CGRP ELISA kit (colorimetric)	Novus	Cat #NBP3-00522
Amylase assay kit (colorimetric)	Abcam	Cat #ab102523
Lipase assay kit (colorimetric)	Abcam	Cat #ab102524
Protein assay dye	Biorad	Cat #5000006
Pierce™ BCA protein assay kit	Thermo Fisher Scientific	Cat #23225
SuperScript VILO cDNA synthesis kit	Thermo Fisher Scientific	Cat #11574050
Fast SYBR green master mix	Applied Biosystems	Cat #4385612
Experimental models: Organisms/strains		
C57BL/6J	The Jackson Laboratory	Cat #000664; RRID: IMSR_JAX:000664
Ai9 (RCL-tdTomato)	The Jackson Laboratory	Cat #007909; RRID: IMSR_JAX:007909

(*Continued on next page*)

Continued

REAGENT or RESOURCE	SOURCE	IDENTIFIER
Cacna2d1$^{fl/fl}$	The Jackson Laboratory	Cat #030704; RRID: IMSR_JAX:030704
$Na_v1.8$-Cre	The Jackson Laboratory	Cat #:036564; RRID: IMSR_JAX:036564
Oligonucleotides		
See Table S2 for primer sequences		N/A
Recombinant DNA		
AAV-tdTomato	Addgene	Cat #105545-AAV1
AAV-eGFP	Addgene	Cat #105530-AAV1
AAV-Cre	Addgene	Cat #105537-AAV1
AAV-Cre-eGFP	Addgene	Cat #105545-AAV1
Software and algorithms		
NIS-Elements imaging software – version 5.11.00	Nikon	https://www.microscope.healthcare.nikon.com/products/software/nis-elements
FIJI (ImageJ)	NIH	https://imagej.net/software/fiji/
GraphPad Prism - version 9.5.1	GraphPad	https://www.graphpad.com
SoftMax PRO 7.1	Molecular Devices	https://moleculardevices.com
Gen 3.10	Agilent BioTEK	https://www.agilent.com/en/support/biotek-software-releases
Cytoscape version 3.10.1	Open source	cytoscape.org
STRING version 12.0	Open source	https://string-db.org/
Other		
Fisherbrand™ Superfrost™ plus microscope slide	Fisher Scientific	Cat #22-037-246
StepOnePlus™ Real-Time PCR system	Thermo Fisher Scientific	Cat #4376600
BIOTEK Synergy H1 microplate reader	Agilent BioTEK	Cat #11-120-535
Spectra MAX190 microplate reader	Molecular Devices	N/A
24-Well Plate (Black)	Sigma Aldrich	Cat #CLS3925
Lysing Matrix D (RNAse-DNAse Free)	MP Biomedicals	Cat #116913050-CF
Bullet Blender®Homogenizer	Next Advance	Cat #BBX24
Sonicator, model 120	Fisher Scientific	Cat #FB120110
Heating block	Fisher Scientific	Cat #88860021
Isotemp oven (model 516G)	Fisher Scientific	Cat #13246516G
Cell strainer, 500 μm	Fisher Scientific	Cat #NC0822591
Cell strainer, 70 μm	Fisher Scientific	Cat #22-363-548
Chambered coverslip (8 wells)	Ibidi	Cat #80806
PVDF membrane, 0.2 μm	Bio-Rad	Cat #1620177
Nitrocellulose membrane, 0.2 μm	Bio-Rad	Cat #1620112

RESOURCE AVAILABILITY

Lead contact

Further information and requests for resources and reagents should be directed to and will be fulfilled by the lead contact, Andrea Tedeschi (andrea.tedeschi@osumc.edu).

Materials availability

This study did not generate new materials.

Data and code availability

This study did not generate any unique datasets or code. Any additional information required to reanalyze the data reported in this paper is available from the lead contact upon request.

EXPERIMENTAL MODEL AND STUDY PARTICIPANT DETAILS

Mice

Adult (8–10 weeks old) female and male C57BL/6J mice (stock no. 000664, RRID: IMSR_JAX:000664) were used for all experiments, except those specifying Ai9 (RCL-tdTomato),[84] $Na_v1.8$-Cre[85] and *Cacna2d1*$^{fl/fl}$[52] mice. Ai9 (RCL-tdTomato) (stock no. 007909; RRID:IMSR_JAX:007909), $Na_v1.8$-Cre (stock no. 036564; RRID:IMSR_JAX:036564) and *Cacna2d1*$^{fl/fl}$ (stock no. 030704; RRID: IMSR_JAX:030704) mice were purchased from The Jackson Laboratory. Mice were randomly assigned to experimental groups. Experimenters were blind to group assignment and experimental conditions. Mice were maintained in a temperature and humidity-controlled facility with a 12-h light/dark cycle. Mice had *ad libitum* access to food and water. All animal experiments were performed following protocols approved by the Institutional Animal Care and Use Committee at The Ohio State University.

DRG neuron culture

Murine DRG neurons were derived from the L3-5 DRG (left side) as described in the method details. Neurons were plated at low density on laminin (5 μg/mL, Roche) coated chambered coverslip with individual wells (Ibidi). The neuronal culture was maintained in a humidified atmosphere containing 5% CO_2 in air at 36.5°C.

Primary adipocyte culture

Primary eWAT adipocytes were derived from adult mice as described in the method details. Matured adipocytes were resuspended in pre-warmed adipocyte culture media (DMEM supplemented with 5% FBS, 5 nM insulin, 1X penicillin/streptomycin) and seeded in a 24-well tissue culture plate containing a poly-D-lysine coated coverslip and incubated at 36.5°C with 5% CO_2.

METHOD DETAILS

Spinal cord injury

Adult mice were anesthetized with a mixture of ketamine (100 mg/kg body weight) and xylazine (10 mg/kg body weight) and a T12 laminectomy was performed. The spinal cord was crushed with modified forceps (no. 5, Cat #11254-20, FST). The forceps were positioned to completely sever ascending dorsal column sensory axons on the left side. For the control surgery, a laminectomy was performed without any direct manipulation of the spinal cord. Mice were allowed to recover for seven days before isolating iWAT and eWAT on the left side for analysis. In another cohort of mice, GBP (46 mg/kg body weight, PHR1049, CAS:60142-96-3, MilliporeSigma) or the corresponding volume of vehicle (0.9% sodium chloride, 0409-7138-09, Aqualite system) was administered (intraperitoneal injections, 3 times/day for the first week, 2 times/day until the end of the study) beginning 1 h after injury. For gradual interruption of the medication (46 mg/kg body weight), the following drug administration regimen was used: 3 times/day for the first week beginning 1 h after injury, 2 times/day for the second week, 1 time/day for the third week and no injections for the fourth week. At 30 days after operation, mice were either transcardially perfused and tissue dissected for further histological analysis, or mice were euthanized and iWAT and eWAT on the left side were isolated for *ex vivo* lipolysis.

Histology and immunohistochemistry

At the end of the study, mice were transcardially perfused with 4% paraformaldehyde (PFA) in PBS (pH 7.4). White adipose tissues were carefully dissected and post-fixed at 4°C in 4% PFA for 24 h. Tissues were paraffin-embedded, sectioned (7 μm thick), and mounted on slides (Comparative Pathology & Digital Imaging Shared Resource, The Ohio State University). Tissue sections were deparaffinized as described elsewhere[86] and subjected to hematoxylin-eosin (HE) staining (ab245880, Abcam) following manufacturer recommendations. When necessary, sections were boiled in citrate-based antigen retrieval solution (pH 6.0, Vector Biolabs) for 10 min using a microwave. After cooling, sections were incubated in 0.5% H_2O_2 for 20 min, followed by blocking at room temperature with 2.5% bovine serum albumin (A3059, Sigma-Aldrich) in PBS with 0.1% Triton X-100 for 1 h and incubated overnight at 4°C with a primary antibody. After washing three times with PBS, sections were incubated with Alexa Fluor–conjugated secondary antibodies (1:400, Life Technologies). Images were taken using a confocal (SP8, Leica; C2 Plus, Nikon) or widefield microscope (Axio Observer Z1, Zeiss). Linear fluorescence intensity was calculated using Fiji (version 2.3.0/1.53f). Analysis of adipocyte morphology in iWAT and eWAT was calculated in ImageJ using the Adiposoft plugin (version 1.16). A manual mode operation was selected. False positive traces were eliminated and missing cells were included in the quantification by tracing the edges of the cells using the free-hand tool. Cells within a single frequency cluster were then divided by the total number of cells to represent the data as frequency distribution (No. of cells in a single bin-size/Total no. of cells X 100). Three-dimensional reconstruction and analysis of eWAT nociceptive nerve terminals in $Na_v1.8$-Cre/Ai9 (RCL-tdTomato) mice were completed using the ImageJ plugin 'SNT'. At least three independent replicates for each condition were analyzed.

Ex-vivo lipolysis

Lipolytic activity in white adipose tissue was performed as described elsewhere.[87] Briefly, eWAT and iWAT (left side) were isolated in Krebs-Ringer bicarbonate buffer (KRBH) (30 mM HEPES, 120 mM NaCl, 1 mM $CaCl_2$, 1 mM $MgCl_2$, 10mM $NaHCO_3$, 4 mM K_2HPO_4) prewarmed at 37°C. Adipose tissue was divided into 30–50 mg specimens and incubated at 37°C in KRBH buffer supplemented with

2% fatty acid-free BSA (A7030, Sigma) with either vehicle (sterile dH_2O) or 10 μM isoproterenol (ab146724, Abcam) for 2 h with constant agitation. In another set of experiments, eWAT depots were incubated at 37°C with either vehicle (sterile dH_2O) or 1 μM CGRP (RP11095, Genscript) for 2 h with constant agitation. Glycerol concentration in the supernatant was determined using a Glycerol Assay Kit (133130, Abcam) following the manufacturer's instructions. Absorbance was collected at 540 nm using a plate reader (Synergy H1, Agilent BioTEK; Spectra Max 190, Molecular Devices). Glycerol concentration was then normalized to the total protein content in the tissue as determined by Pierce BCA Protein Assay Kit (23225, Thermo Fisher Scientific) or Bio-Rad Protein Assay Dye Reagent (5000006, Bio-Rad).

Immunoblotting

Adipose tissues were dissected at 7 or 30 days after the operation (sham and SCI), collected in DNAse-RNAse free Lysing Matrix D tubes (2 mL) containing zirconium beads (1.4 mm diameter) and lysed in 6 volumes of ice-cold RIPA buffer (50mM Tris, pH 7.5, 150mM NaCl, 1% IGEPAL CA-630, 1% Triton X-100, 0.2% SDS, 0.5% sodium deoxycholate, 2mM EDTA) containing phosphatase and protease inhibitors (Roche). Tissue samples were homogenized using a bullet blender homogenizer (Storm Pro, Next Advance) for 5 min (speed #6) followed by incubation in ice for 60 min. Samples were then transferred into new tubes, and centrifuged at 6000 g for 15 min at 4°C, followed by two cycles of 20000 g for 30 min at 4°C. Lipid-free tissue lysates were collected into pre-chilled 1.5 mL tubes and protein concentration was then determined using Pierce BCA Protein Assay Kit (Thermo Fisher Scientific, 23225) or Bradford Protein Assay (5000006, Biorad). A portion of the lysate (10–20 μg) was then fractionated by sodium dodecyl-sulfate–polyacrylamide gel electrophoresis. The separated proteins were transferred to a 0.2 μm PVDF or nitrocellulose membrane (Bio-Rad) that was stained to confirm equal loading and transfer of the samples with Ponceau S (P7170, Millipore Sigma). After blocking at room temperature with 5% non-fat milk (1706404, Bio-Rad) in Tris-buffered saline with 0.1% Tween 20 detergent for 1 h, the membrane was probed with rabbit monoclonal antibody anti-ATGL (1:1000), *p*-HSL (1:1000) or HSL (1:1000). Rabbit monoclonal anti-GAPDH (1:4000) antibodies were used as the loading control. Densitometry analysis was performed using ImageJ (NIH). After background subtraction, the intensity of ATGL, *p*-HSL and HSL bands was measured and normalized to the loading control (e.g., GAPDH). A minimum of three biological replicates for each experimental condition were analyzed.

Circulating catecholamines, glycerol and free fatty acids in the serum

Mice were euthanized and blood samples were taken from the heart via cardiac puncture. Samples were incubated at room temperature for 30 min allowing blood to clot and then centrifuged at 4°C for 15 min at 2500 rpm. Serum samples were transferred to new tubes. Catecholamines, glycerol and free fatty acids were determined using commercial kits following the manufacturer's guidelines.

AAV injection and transduction of DRG neurons *in vivo*

AAV particles expressing tdTomato (Addgene), eGFP (Addgene), Cre or Cre-eGFP (Addgene) were injected into the left sciatic nerve (2 μL/mouse) of adult wild-type, Ai9 (RCL-tdTomato) or *Cacna2d1*$^{fl/fl}$ mice. In a separate cohort of Ai9 (RCL-tdTomato) mice, AAV-Cre-eGFP was injected directly into L4 DRG. Two weeks after the AAV injection, the left eWAT was isolated for *ex vivo* lipolysis or histological analysis. L3-5 DRGs were collected to verify changes in *Cacna2d1* expression. Two weeks after AAV injections, another cohort of adult *Cacna2d1*$^{fl/fl}$ mice was subjected to a T12 SCI. Seven days after SCI, eWAT was isolated for *ex vivo* lipolysis and histological analysis.

Fluoro-Gold retrograde tracing

A small incision was made in the lower left quadrant of the abdomen of adult wild-type mice, and Fluoro-Gold tracer (1%, Fluorochrome) was injected (1 μL/spot, 4 spots) into the left eWAT. In another cohort of adult wild-type mice, a T12 SCI was performed and four days later, 1% Fluoro-Gold was injected (500 nL, 1 spot) at the lesion site. Three days after tracer injection, the mice were perfused and lumbar L3-5 DRG dissected and sequentially dehydrated in 10%, 20%, and 30% sucrose. Tissues were then embedded in optimum cutting temperature (OCT) compound (Tissue-Tek), frozen, sectioned (14 μm thick, HM525 NX, Thermo Fisher Scientific), and mounted on slides. Slides were warmed at 37°C for 30 min and OCT was washed away with PBS. Sections were then blocked at room temperature with 2.5% bovine serum albumin (A3059, Sigma-Aldrich) in PBS with 0.1% Triton X-100 for 1 h and incubated overnight at 4°C with the primary antibody. After washing 3 times with PBS, sections were incubated with Alexa Fluor–conjugated secondary antibodies (1:500, Life Technologies). Images were taken using a confocal (C2 plus, Nikon) or epifluorescence microscope (Axio Observer Z1, Zeiss). The expression of CGRP, $\alpha2\delta1$ and $\alpha2\delta2$ in Fluoro-Gold–labeled DRG neurons was measured by using Zen Blue software (Zeiss). A minimum of 3 independent biological replicates (2-3 sections/mouse) were analyzed per condition.

DRG neuron culture

Seven days after sham and SCI, L3-5 DRG (left side) were dissected from $Na_v1.8$-Cre/Ai9 (RCL-tdTomato) and collected in ice-cold Hank's balanced salt solution (HBSS, GIBCO). After removing the surrounding connective tissue, the ganglia were transferred into a sterile tube and washed twice with HBSS. The ganglia were incubated in Neurobasal-A medium (GIBCO) containing collagenase type I (3,000 U/mL, Worthington) at 36.5°C for 15 min, followed by 30 min with trypsin (0.25%, GIBCO). Serum was then added to stop trypsin digestion. Ganglia were dissociated by gently pipetting up and down. The cell suspension was filtered using a nylon cell strainer (70 μm, Fisher Scientific) and centrifuged at 900 rpm for 5 min. Dissociated neurons were re-suspended in Neurobasal-A

medium supplemented with B-27 (GIBCO) and were plated at low density on laminin (5 μg/mL, Roche) coated chambered coverslip with individual wells (Ibidi). The neuronal culture was maintained in a humidified atmosphere containing 5% CO_2 in air at 36.5°C. Neurons were fixed 48 h after plating. Axon length and branching frequency were calculated using Fiji. Cav2.1 expression in tdTomato positive DRG neurons was calculated using the Zen Blue software (Zeiss).

Primary adipocyte culture and calcium imaging

Primary adipocyte culture was performed as described elsewhere.[88] Briefly, murine eWAT was dissected, rinsed in sterile DPBS w/o Ca^{2+} and Mg^{2+} and chopped into small pieces. The tissue was then transferred into a sterile 50 mL tube and digested at 36.5°C for 1 h in collagenase buffer (Gey's balanced salt solution containing 10 mg/g of Collagenase Type I, 10mM HEPES, 1% BSA, and 50 μM Adenosine) under constant agitation. The digested tissue was filtered using a 500 μm cell strainer and centrifuged at 4°C for 10 min at 1000 rpm. After carefully removing the lipid layer on the top, matured adipocytes were collected in a sterile 15 mL tube and resuspended in 4 volumes of wash buffer (DPBS w/o Ca^{2+} and Mg^{2+} containing 0.1% BSA and 5 mM EDTA). Cells were centrifuged at 4°C for 7 min at 400 g, and the wash step was repeated. After removing the wash buffer, matured adipocytes were resuspended in pre-warmed adipocyte culture media (DMEM supplemented with 5% FBS, 5 nM insulin, 1X penicillin/streptomycin). An equal number of cells was seeded in a 24-well tissue culture plate containing a poly-D-lysine coated coverslip and incubated at 36.5°C with 5% CO_2. The following day, matured eWAT adipocytes were used for calcium imaging. Cells were loaded with the cell-permeant calcium indicator Fluo-4 AM (5 μM) at 36.5°C for 45 min. The medium was then replaced with a pre-warmed culture medium and eWAT adipocytes were loaded on a custom chamber suited for time-lapse imaging. Time-lapse imaging was conducted over a period of 60 s (exposure: 200 ms; time interval: 3 s). After collecting baseline values over a period of 15–30 s, CGRP (43 μM) was then added to the cell suspension using a micropipette while repetitive imaging continued. A time stamp was used to determine when CGRP was added to the medium. Imaging data were analyzed using ImageJ (NIH). After background subtraction, the fluorescence signal of individual adipocytes was measured frame by frame. The mean values were then normalized to each baseline (e.g., w/o CGRP) and data were plotted using Igor Pro (version 8, WaveMetrics). The peak amplitude of the calcium response for each adipocyte was measured and expressed as $\Delta F/F$.

Laser speckle imaging

To monitor changes in eWAT blood perfusion, mice were subjected to a T12 SCI and sham operation. Seven days later, mice were anesthetized and transferred to a stereotaxic frame. After performing a midline incision to expose eWAT, mice were positioned under the laser speckle contrast imaging system (RFLSI II, RWD), and the eWAT surface was illuminated with a 784-nm laser (60 mW). Blood flow was recorded for 10 s (4.8X, 2048 x 2048, 10 frames at 10 Hz with 2 ms exposure time). Data analysis was performed using dedicated software (RWD Life Science).

Vasculature tracing, 3D imaging and reconstruction

The eWAT vasculature was traced using the method we described earlier.[21] Briefly, mice were transcardially perfused with 4% PFA in PBS (pH 7.4). Mice were then perfused with 5 mL of 0.05% albumin-tetramethylrhodamine isothiocyanate bovine (A2289, Sigma) in 2% gelatin from porcine skin (G1890, Sigma). At the time of injection, the temperature of the gel solution was maintained at 45°C. After clamping the heart, mice were placed on ice to lower their body temperature and allow for gel formation. The eWAT (left side) was dissected and cleared using the advanced CUBIC protocol[89] and imaged in 3D using a confocal microscope (C2 plus, Nikon). Vasculature networks were reconstructed and analyzed using the 3D image software Imaris (version 10.0.0, Andor Technology).[73] Results were further validated using the ImageJ plugin 'SNT'.

Flow cytometry

Flow cytometric analysis was performed as previously described.[90] The cells were labeled with fixable viability dye (eFluor506 or eFluor780; eBioscience), blocked with anti-CD16/32 (clone 2.4G2), and stained with fluorochrome-conjugated antibodies specific for CD11b (clone M1/70), Ly6G (1A8), CD45 (30-F11), CD14 (rmC5-3), CD115 (T38-320), I-A/I-E (M5/114.15.2), CD64 (X54-5/7.1), Ly6C (AL-21), F4/80 (T45-2342), and CD11c (HL3), which were all purchased from BD Pharmingen, and MerTK (DS5MMER) was purchased from Invitrogen. For intracellular staining, the cells were fixed and permeabilized with BD cytofix and cytoperm solutions and then stained with fluorescent antibodies specific for arginase-1 (polyclonal; R&D) and CD206 (MR6F3; eBiosciences). Flow cytometry was performed with a FACS Symphony A3 cell analyzer (BD Biosciences). The cells were gated on forward and side scatter after double exclusion and analyzed on FlowJo software (version 10, BD Biosciences).

RNA Isolation and real-time PCR

Two weeks after AAV-eGFP or AAV-Cre-eGFP injection into the left sciatic nerve, total RNA was extracted from L3-5 DRG using the RNeasy kit (Qiagen) and cDNA was synthesized from 0.1 to 0.5 μg of RNA using the SuperScript VILO cDNA synthesis kit (11754050, Thermo Fisher Scientific). In separate experiments, eWAT was collected 7 days after SCI and sham operation and total RNA extracted as described above. The subsequent cDNA was used in a real-time PCR (StepOne Plus, Applied Biosystem) using Fast SYBR Green Master Mix (4385612, Applied Biosystem). Melting curve reactions were run with each primer set. The *β actin* gene was used for normalization. The sequences of the primers used are listed in Table S2.

Normalized expression was calculated as ΔCt (gene norm) = Ct *Cacna2d1* – Ct *βactin* and normalized expression = $2^{-\Delta Ct}$ (gene norm). After calculating the average expression for each gene across all samples, a *Z* score ($Z = (X - \mu)/\sigma$, μ = mean, σ = standard deviation) was generated for each biological replicate. A heatmap was used to display differential gene expression across the three experimental conditions.

α2δ1 knockdown efficiency

Three weeks after AAV-GFP or AAV-Cre-eGFP injection into the left sciatic nerve, adult *Cacna2d1*$^{fl/fl}$ mice were transcardially perfused with 4% PFA in PBS (pH 7.4). L3-5 DRG were dissected and post-fixed at 4°C in 4% PFA for 2 h. Tissues were cryoprotected at 4°C in 30% sucrose for 48 h. Cryosections (10 μm thick) were mounted on slides. Sections were incubated at room temperature with 2.5% bovine serum albumin (A3059, Sigma-Aldrich) in PBS with 0.1% Triton X-100 for 1 h and then incubated with a rabbit antibody (Sigma) directed against α2δ1 for 2 h. After washing three times with PBS, sections were incubated at room temperature with Alexa Fluor–conjugated secondary antibody (1:400, Life Technologies) for 1 h. Sections were then washed three times with PBS and coverslips were mounted. Images were taken using a confocal microscope (C2 Plus, Nikon). Linear fluorescence intensity and area of the neuronal cell body of virally transduced L3-5 DRG neurons were calculated using Fiji (version 2.3.0/1.53f).

CGRP levels in eWAT and serum

CGRP content was calculated using the Mouse CGRP ELISA kit (NBP3-00522, Novus Biologicals) following the manufacturer's instructions. Briefly, eWAT samples were lysed in 9 volumes of ice-cold PBS (pH 7.4) using DNAse-RNAse free Lysing Matrix D tubes (2 mL) in a bullet blender homogenizer. Tissue lysates were sonicated (10 s pulse at 80% power) (Model 120, Thermo Fisher Scientific) and centrifuged at 4°C for 30 min at 20,000 g. The centrifugation step was repeated twice to eliminate lipid contamination. The lysates were diluted 10 times and CGRP concentration was calculated according to the manufacturer's instructions. CGRP levels were then normalized to the total protein content in the tissue. To determine CGRP levels in the serum, undiluted serum samples were assessed using the same ELISA kit.

EchoMRI

Murine lean and fat mass was determined using Echo-MRI-4in1 Body Composition Analyzer (EchoMRI, LLC).

Oil red O staining

Accumulation of neutral lipids in the liver was assessed by oil red O staining as described elsewhere.[91] Liver sections (14 μm thick) were incubated at room temperature for 10 min with oil red O working solution. Sections were then rinsed with distilled water and mounted using a water-soluble mounting medium. Bright-field images were acquired using a light microscope (Zeiss). A minimum of three images per biological replicate were analyzed and the intensity of red O stain was measured using ImageJ.

Insulin and glucose tolerance test

After 6 h of fasting, the baseline blood (tail bleeding) glucose level was determined using a standard glucometer (Contour Plus, Bayer) for both insulin and glucose tolerance tests. For the insulin tolerance test, mice were intraperitoneally injected with insulin (Humulin R, Thermo Fisher Scientific) at a dose of 0.75U/kg body weight, and blood glucose was determined at different time points over a 90-min period. The blood glucose level at each time point was expressed as a percentage of the baseline glucose level. For the glucose tolerance test, mice were intraperitoneally injected with D-(+)-glucose (G8270, Sigma-Aldrich) at a dose of 1 g/kg body weight, and blood glucose was determined at different time points for 120 min.

Pancreas histology, amylase and lipase activity

Basal pancreatic amylase and lipase activity was measured using Amylase Assay Kit (ab102523, Abcam), and Lipase assay kit (ab102524, Abcam) respectively. Briefly, ∼30mg of murine pancreas were dissected, snap frozen in liquid nitrogen and stored in −80°C. Before the assay, tissues were thawed in ice and homogenized using a Dounce tissue grinder (15 passes) and the buffer provided in the kits. The tissue lysates were centrifuged at 20,000g for 5 min at 4°C. Amylase and lipase activity was measured following the manufacturer's recommendation.

Indirect calorimetry

Metabolic parameters were measured using indirect calorimetry in open-circuit Oxymax chambers in the Comprehensive Lab Animal Monitoring System (CLAMS) (Columbus Instruments). Mouse were individually housed in the chambers at 22°C with 12-h light/12- hour dark cycle, with *ad-libitum* access to food and water. VO_2, VCO_2, RER (VCO_2/VO_2) were acquired every 15 min over the course of 48 h. The data collected in the first 10–12 h were not used for analysis as mice were allowed to acclimate to the new environment. The datasets from different experimental conditions were synchronized (all starting at 6 p.m. at the beginning of the dark cycle) and all data points were used for analysis.

Prediction of protein-protein interaction network

The list of DEG shared among *Cacna2d1* conditional deletion and GBP administration was imported to STRING.[92] The file network was then exported to Cytoscape[93] for visualization. Recentering the network on each of the three DEG shared among all experimental conditions allows to visualize first neighbors.

QUANTIFICATION AND STATISTICAL ANALYSIS

Statistical analysis was performed using SAS (SAS 9.4; SAS Institute) and Prism (version 9.3.1; GraphPad) and included: two-way ANOVA, mixed model with a random subject intercept to account for within-subject correlation, unpaired 2-tailed Student's t test, paired 2-tailed Student's t test, two-sample Kolmogorov-Smirnov test and Kruskal-Wallis test followed by Dunn's multiple comparisons test. For all analyses performed, significance was defined as $p < 0.05$. The type of analysis for each dataset, the exact values of n and the definition of measures are shown in the corresponding figure legends.